J. Fluid Mech. (1995), vol. 300, pp. 231–263

Collective hydrodynamics of deformable drops and bubbles in dilute low Reynolds number suspensions

By MICHAEL MANGA[1]† AND H. A. STONE[2]

[1]Department of Earth and Planetary Sciences, Harvard University, Cambridge, MA 02138, USA
[2]Division of Applied Sciences, Harvard University, Cambridge, MA 02138, USA

(Received 13 June 1994 and in revised form 28 November 1994)

Deformation due to hydrodynamic interactions between two deformable buoyant drops may result in the alignment and coalescence of horizontally offset drops. Three-dimensional boundary integral calculations are presented for systems containing two, three or four drops and it is argued that the interactions which occur between three drops or four drops may be characterized qualitatively by the two-drop interactions. In a dilute monodisperse suspension, the rate of coalescence of deformable drops is calculated using far-field analytical results and is found to be proportional to the Bond number. The rate of coalescence in a dilute polydisperse suspension of bubbles in corn syrup is determined by performing a large number of laboratory experiments for Bond numbers based on the larger bubble radius $15 < \mathscr{B} < 120$. The rate of coalescence is enhanced (by a factor of 10 for $\mathscr{B} = 10$), owing to the effects of deformation, compared to the predictions of models which include hydrodynamic interactions and van der Waals forces among spherical bubbles. The rate of coalescence is greater than the rate predicted by the Smoluchowski model which ignores *all* hydrodynamic interactions. The experimental results are used to calculate the evolution of the bubble size distribution in suspensions using a standard one-dimensional population dynamics model; deformation affects the size distribution in suspensions, resulting in a wider range of bubble sizes.

1. Introduction

We are interested in studying the rate of coalescence of deformable particles in a suspension in order to calculate macrophysical properties such as the particle size distribution and the average sedimentation rate. A typical approach to calculating macrophysical properties involves using population dynamics models which require an understanding of the interactions among the many particles in the suspension. The detailed hydrodynamic interactions and physicochemical effects among particles are microphysical properties which govern coalescence. Previous theoretical studies of low Reynolds number dilute suspensions of spherical particles have considered the interactions due to Brownian motion and van der Waals forces, gravitational settling (Zhang & Davis 1991), interfacial tension variations due to surfactant or

† Now at Department of Geology and Geophysics, University of California, Berkeley.

thermocapillary effects (Satrape 1992; Zhang & Davis 1991), or a combination of the above (e.g. Zhang, Wang & Davis 1993).

We extend the above studies by considering the effects of deformation on the evolution of particle size and concentration in dilute suspensions of buoyant particles. Deformation is characterized by the Bond number

$$\mathscr{B} = \frac{\Delta\rho g a^2}{\sigma}, \tag{1.1}$$

where a is a particle radius, $\Delta\rho$ is the density difference between the particle and the external fluid, σ is the interfacial tension, and g is the gravitational acceleration. The Bond number represents the ratio of buoyancy forces to interfacial tension forces. We assume that the Reynolds number is small,

$$\mathscr{R} = \frac{\rho U a}{\mu} \ll 1, \tag{1.2}$$

where ρ and μ are the external fluid density and viscosity, respectively, and U is the particle's translational speed. Manga & Stone (1993) have shown that deformation has a significant effect on low Reynolds number drop interactions for $\mathscr{B} > O(1)$. We also assume that the Péclet number is large so there is negligible Brownian motion. Other effects such as Ostwald ripening and interfacial tension variations are neglected.

1.1. *Interactions between two deformable drops and bubbles*

The interactions between two drops model many two-body interactions common to multiphase sedimentation processes – a quantitative understanding of two-particle interactions is the starting point for theoretical studies which attempt to characterize the behaviour (e.g. sedimentation rate and coagulation rate) of suspensions. Manga & Stone (1993) presented photographs of experimental results and two-dimensional numerical calculations which demonstrated that two deformable, horizontally offset, buoyant drops or bubbles interact in a manner which promotes vertical alignment and coalescence. In figure 1 we present two sequences of photographs, similar to those presented in Manga & Stone (1993), which illustrate two distinct ways in which offset air bubbles may interact in a Newtonian fluid at small Reynolds numbers ($\mathscr{R} \approx 10^{-3}$) and large Bond numbers ($\mathscr{B} \approx 20$). The experiment in figure 1(a) illustrates a process we refer to as *coating*, in which the smaller leading bubble spreads over the surface of the larger trailing bubble. The experiment in figure 1(b) illustrates a different process we refer to as *entrainment*, in which the smaller bubble is advected around the larger bubble and is 'sucked' or entrained into the larger bubble. Coalescence occurs between the last two photographs shown in (a) and shortly after the last photograph shown in sequence (b). The difference between the two experiments is that the initial horizontal separation distance is sufficiently large in figure 1(b) that coating does not occur. Clearly, for sufficiently large horizontal offsets, the smaller bubble does not coalesce with the larger bubble.

The importance of deformation on drop dynamics at low Reynolds number may be highlighted by noting that for two spherical particles, observed relative to the larger one, the smaller sphere is advected around the larger sphere, as illustrated in figure 2(a). A qualitative explanation for the alignment of deformable offset bubbles (figure 1a) is illustrated schematically in figure 2(b). Alignment occurs since the effect of hydrodynamic interactions is to deform the trailing bubble into a prolate shape, suitably inclined with respect to the vertical; the leading bubble

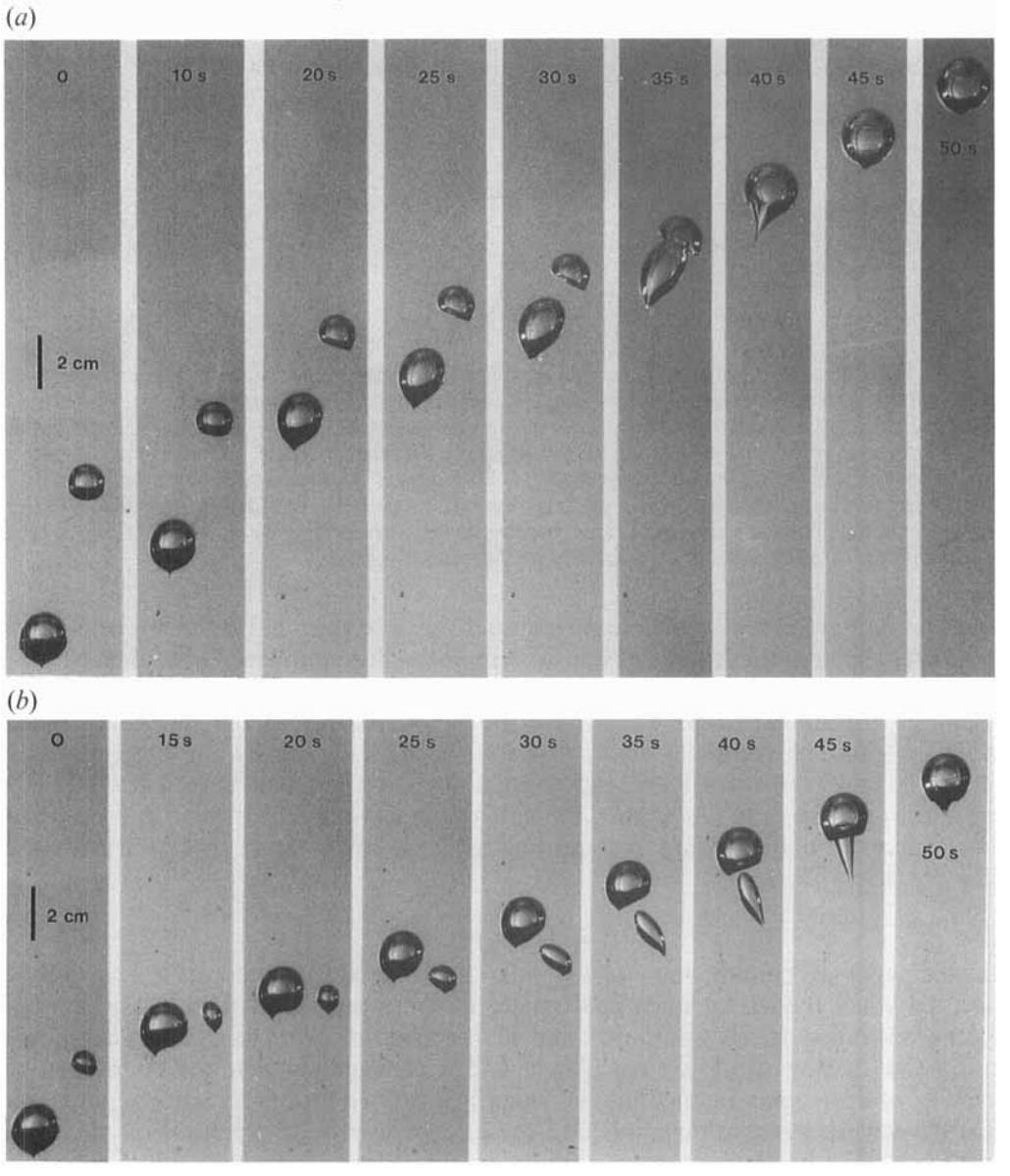

FIGURE 1. Interaction and deformation of two air bubbles rising in a large container of corn syrup: (*a*) alignment and (*b*) 'suction' or entrainment of bubbles which are initially horizontally offset. The Reynolds number $\mathscr{R} \approx 10^{-3}$ and the Bond number $\mathscr{B} \approx 20$. Times and a scale bar are shown on the photographs. Coalescence occurs between the last two photographs shown in (*a*) and shortly after the last photograph shown in sequence (*b*).

is deformed into an oblate shape. The inclined shapes lead to small horizontal components of translation which tend to align the bubbles. Thus, even equal-sized deformable bubbles interact in a manner leading to eventual coalescence. The second type of two-bubble interaction (figure 1*b*), in which the small bubble is first advected around the larger bubble and then sucked in from behind, arises due to the deformation of the larger bubble. The entrainment dynamics result from the continual deformation of the larger bubble so that in a frame of reference moving

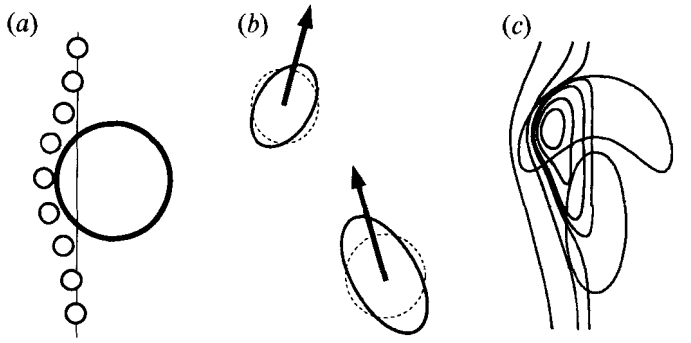

FIGURE 2. (*a*) Illustration of the interaction of spherical particles: relative to the larger sphere, the small sphere is swept around the larger one. (*b*) Illustration of the alignment process: undeformed spherical shapes are shown with dashed curves and deformed shapes are shown with solid curves. The stress field produced by one particle deforms the other particle leading to a horizontal component of translation and thus alignment. (*c*) Streamlines, calculated relative to the larger drop, for a pair of translating and deforming axisymmetric drops. The calculation uses the boundary integral method. The drops have the same viscosity as the surrounding fluid; $\mathscr{B} = 50$. This figure is a compilation of results presented originally in Manga & Stone (1993).

with the larger bubble, streamlines intersect the interface and a vortex or wake is generated behind the bubble (even at zero Reynolds numbers). To illustrate this mode of interaction, in figure 2(*c*) we show numerically computed streamlines for a pair of translating drops which have the same viscosity as the surrounding fluid and $\mathscr{B} = 50$. The continual deformation at the back of the leading drop results in closed streamlines which leave and re-enter the drop defining a vortex which may entrain a trailing drop. At higher Reynolds numbers alignment may also occur for two spherical bubbles owing to the formation of a low-pressure wake (de Nevers & Wu 1971).

1.2. *Paper overview*

In this paper we employ numerical simulations, laboratory experiments and population dynamics models to study coalescence of drops and bubbles in suspensions. In §2 the buoyancy-driven translation and deformation of drops in systems containing two, three or four drops are calculated, and it is suggested that the interactions in 'clouds' of drops may be qualitatively described by two-drop interactions. A theoretical framework suitable for modelling coalescence in dilute suspensions is described in §3, and the coalescence rate, accounting for deformation, in a dilute monodisperse suspension is derived in §4. Next, in §5, the coalescence rate of bubbles in a dilute polydisperse suspension is determined experimentally as a function of the Bond number and relative bubble sizes. Finally, in §6, a one-dimensional population dynamics model is used to calculate typical bubble size distributions in suspensions. We demonstrate that deformation has two effects: first, the rate of coalescence is increased, as suggested from the experimental results shown in figure 1, and second, the size distribution is characterized by a wider range of sizes if the dispersed phase is allowed to deform.

2. Two drops, three drops and four drops

In this section we consider numerically the interaction of pairs of three-dimensional offset drops. We then consider the interaction among drops in systems containing

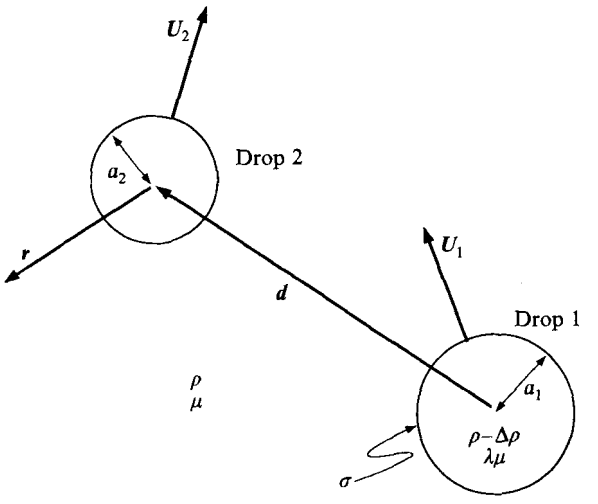

FIGURE 3. Two-drop geometry.

three and four drops. The results demonstrate that two-drop dynamics qualitatively describe the interactions in systems with more than two drops. We begin with a short scaling analysis which will allow us to better understand some of the features characteristic of drop interactions and deformation.

2.1. *Scaling analysis*

Consider two spherical drops with radii a_1 and a_2, separated by distance d, with $d/a \gg 1$, as shown in figure 3, where a with no subscript denotes a typical radius. Each drop rises, to a first approximation, as though alone in an unbounded fluid. The rise speed of drop i as a function of the viscosity ratio λ is given by the Hadamard–Rybczyński result

$$\boldsymbol{U}_i^{(0)} = -\frac{2(1+\lambda)}{3(2+3\lambda)}\frac{\Delta\rho a_i^2}{\mu}\boldsymbol{g}, \qquad i = 1,2. \tag{2.1}$$

Each drop creates a velocity field

$$\boldsymbol{u}_i^{(0)}(\boldsymbol{r}) = \frac{2\pi(2+3\lambda)}{(1+\lambda)}a_i\left[1+\frac{\lambda a_i^2}{2(2+3\lambda)}\nabla^2\right]\boldsymbol{J}\cdot\boldsymbol{U}_i^{(0)} \tag{2.2}$$

where

$$\boldsymbol{J}_i(\boldsymbol{r}) = \frac{1}{8\pi}\left(\frac{\boldsymbol{I}}{r}+\frac{\boldsymbol{rr}}{r^3}\right). \tag{2.3}$$

To leading order, the correction to the rise speed of each particle is described by the first reflection (a 'push' on the leading drop by the trailing drop and a 'pull' on the trailing drop by the leading drop). The additional speed of drop 1, δU_1, due to the second particle is given by

$$\delta U_1 = O\left(\frac{\Delta\rho g a_2^3}{\mu d}\right) \tag{2.4}$$

and the additional speed of drop 2, δU_2, is

$$\delta U_2 = O\left(\frac{\Delta\rho g a_1^3}{\mu d}\right). \tag{2.5}$$

The velocity field created by a translating drop, described by equations (2.2) and (2.3), creates velocity gradients which deform nearby drops. Let ϵ_i measure the small distortion away from a spherical shape, and let $\mathscr{B}_i = \Delta\rho g a_i^2/\sigma$ be the Bond number for drop i. The far-field velocity gradient generated by drop 1 in the vicinity of drop 2 is $O(U_1 a_1/d^2)$. A balance of viscous stresses, $O(\mu U_1 a_1/d^2)$, by the interfacial tension stresses of drop 2, $O(\epsilon_2\sigma/a_2)$, which tend to keep the drop nearly spherical, leads to a small shape distortion of drop 2 with magnitude

$$\epsilon_2 = O\left(\frac{a_1^3 a_2 \Delta\rho g}{\sigma d^2}\right) = O\left(\mathscr{B}_2 \frac{a_1}{a_2}\left(\frac{a_1}{d}\right)^2\right). \tag{2.6}$$

A similar analysis for drop 1 gives

$$\epsilon_1 = O\left(\frac{a_1 a_2^3 \Delta\rho g}{\sigma d^2}\right) = O\left(\mathscr{B}_1 \frac{a_2}{a_1}\left(\frac{a_2}{d}\right)^2\right). \tag{2.7}$$

Since the magnitude of deformation is $O(\mathscr{B}a^2/d^2)$, it follows that the correction to the rise speed is $O(U^{(0)}\mathscr{B}a^2/d^2)$, where $U^{(0)}$ is the Hadamard–Rybczyński rise speed. Also, the relative magnitude of distortion of the two drops is

$$\frac{\epsilon_1}{\epsilon_2} = \left(\frac{a_2}{a_1}\right)^2. \tag{2.8}$$

Thus, (surprisingly) the smaller drop will be more deformed than the larger drop, as seen in the experiments shown in figure 1.

2.2. *The boundary integral method*

The numerical solution of three-dimensional free-boundary problems is difficult; most previous studies for either low or high Reynolds numbers have focused on a single deformable drop or bubble (although Unverdi & Trygvasson 1992 have studied interactions between two drops). Previous low Reynolds number studies have considered the deformation of neutrally buoyant drops in shear flows in the limit of modest shape distortions (e.g. Rallison 1981; Kennedy, Pozrikidis & Skalak 1993; deBruijn 1989). Below we present three-dimensional numerical calculations of the buoyancy-driven translation of multiple drops which we believe are the first for low Reynolds number buoyancy-driven interactions, and the first simulations to consider large interface distortions. The numerical method involves discretizing the drop surfaces by a mesh of 3200 triangular surface elements and a grid of 382 collocation points. Details of the numerical procedure and implementation are discussed in Appendix A. Since the three-dimensional calculations are computationally intensive, the calculations reported here took 5–10 days on a Sparc 2 workstation, calculations are performed for drops with the same viscosity as the surrounding fluid ($\lambda = 1$). The Bond number reported is based on the radius of the larger trailing drop, time is normalized by an advective timescale, $\mu/\Delta\rho g a_1$, where a_1 is the radius of the larger drop, and lengths are scaled by a_1.

2.3. *Two drops*

In figures 4–6 we show cross-sections of the interface shapes for buoyant translating drops at different times. Figure 4 shows the effects of changing the Bond number; figure 5 shows the effect of the initial horizontal offset (i.e. the horizontal distance

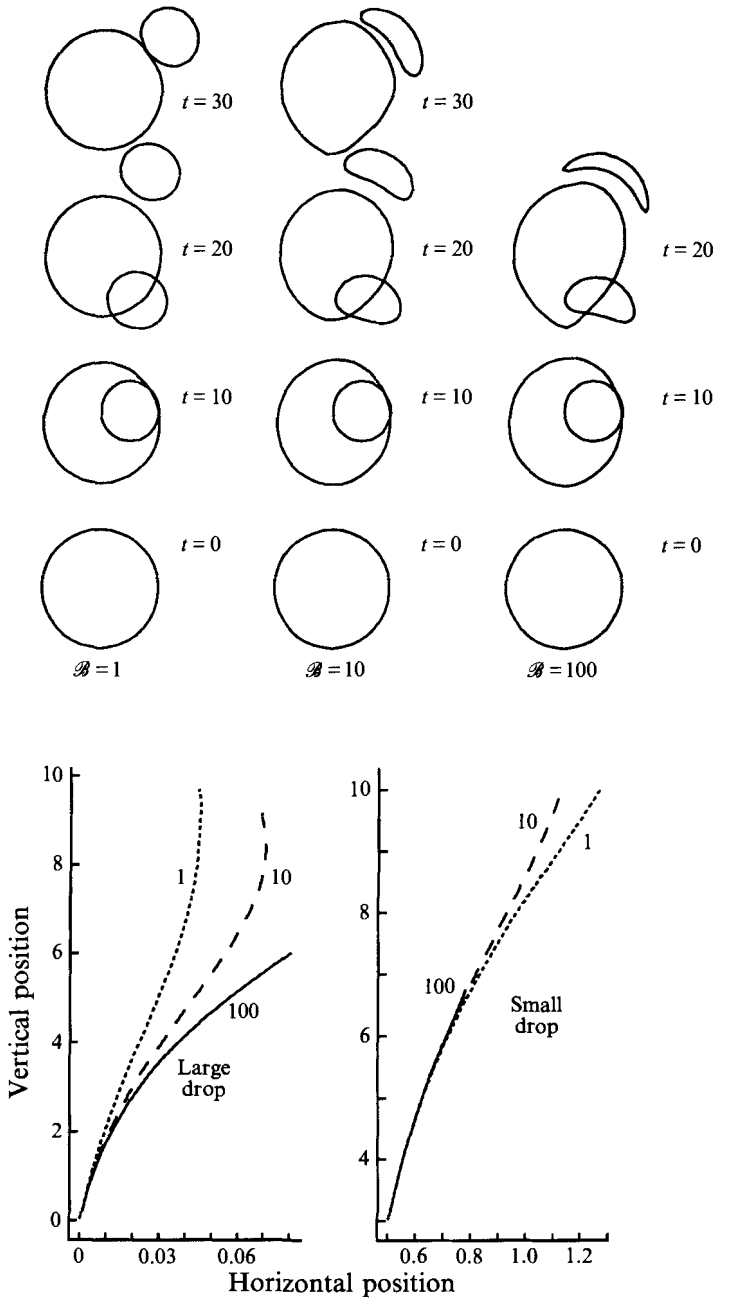

FIGURE 4. The effect of interfacial tension (Bond number) on the alignment of three-dimensional offset drops for Bond numbers of the larger trailing drop $\mathscr{B} = 1$, 10 and 100 ; $\lambda = 1$, $a_2/a_1 = 0.5$. Cross-sections of three-dimensional shapes are shown. Drop trajectories are shown in the lower figure. Time is normalized by an advective timescale, $\mu/\Delta\rho g a_1$, where a_1 is the radius of the larger drop.

between centres of mass); figure 6 shows the effect of the relative drop size. Corresponding to the simulations shown in figures 4–6, trajectories of the centres of mass of the two drops are also presented, which allows an improved quantitative understanding of the importance of deformation and relative drop orientation.

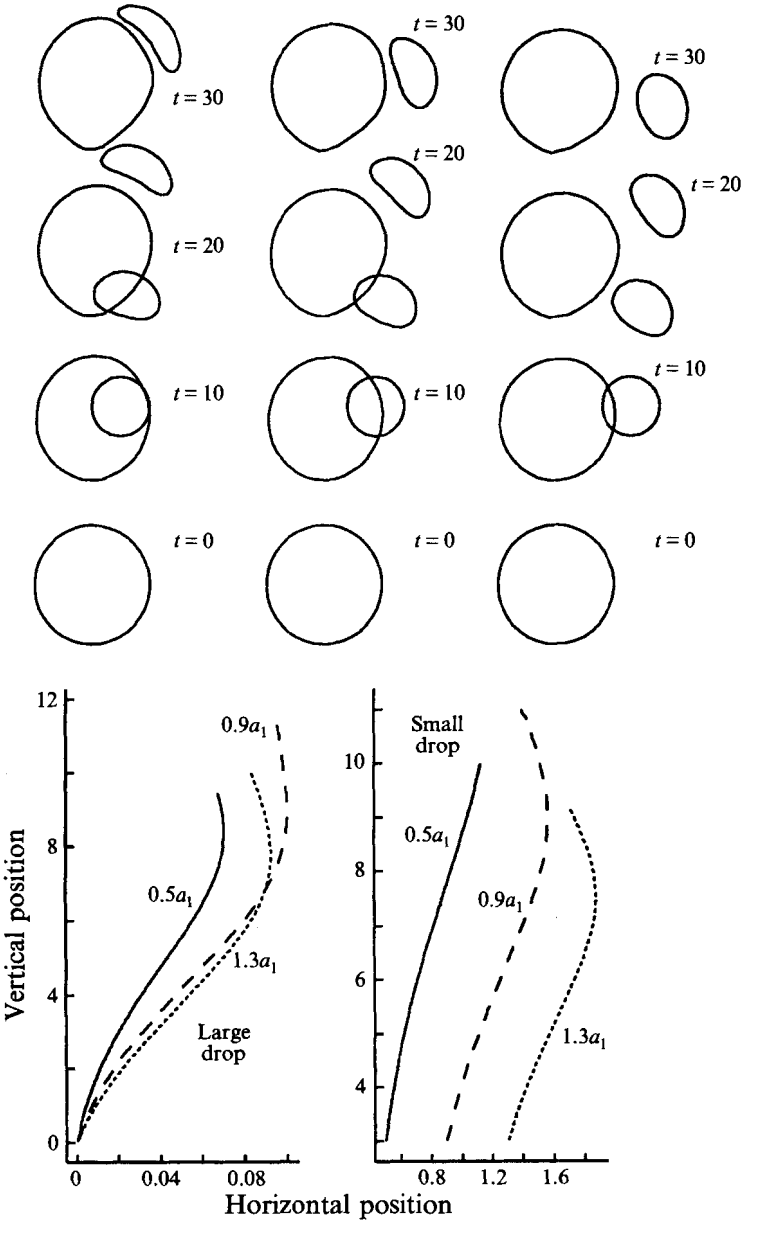

FIGURE 5. The effect of initial horizontal offset on the alignment of three-dimensional offset drops for initial horizontal offsets of $0.5a_1$, $0.9a_1$ and $1.3a_1$; $\mathscr{B} = 10$, $\lambda = 1$, $a_2/a_1 = 0.5$ (Bond number based on the radius of the larger drop). Cross-sections of three-dimensional shapes are shown. Drop trajectories are shown in the lower figure.

2.4. *Effects of interfacial tension (Bond number)*

In figure 4 we present three simulations for the same initial condition but different Bond numbers: $\mathscr{B} = 1$, 10 and 100, $\lambda = 1$, and $a_2/a_1 = 0.5$. For $\mathscr{B} = 1$ the drops remain nearly spherical and the small drop does not coat the larger drop, whereas for $\mathscr{B} = 100$ the small drop is flattened by the trailing drop and coating occurs. The thickness of the fluid film trapped between the drops also decreases most

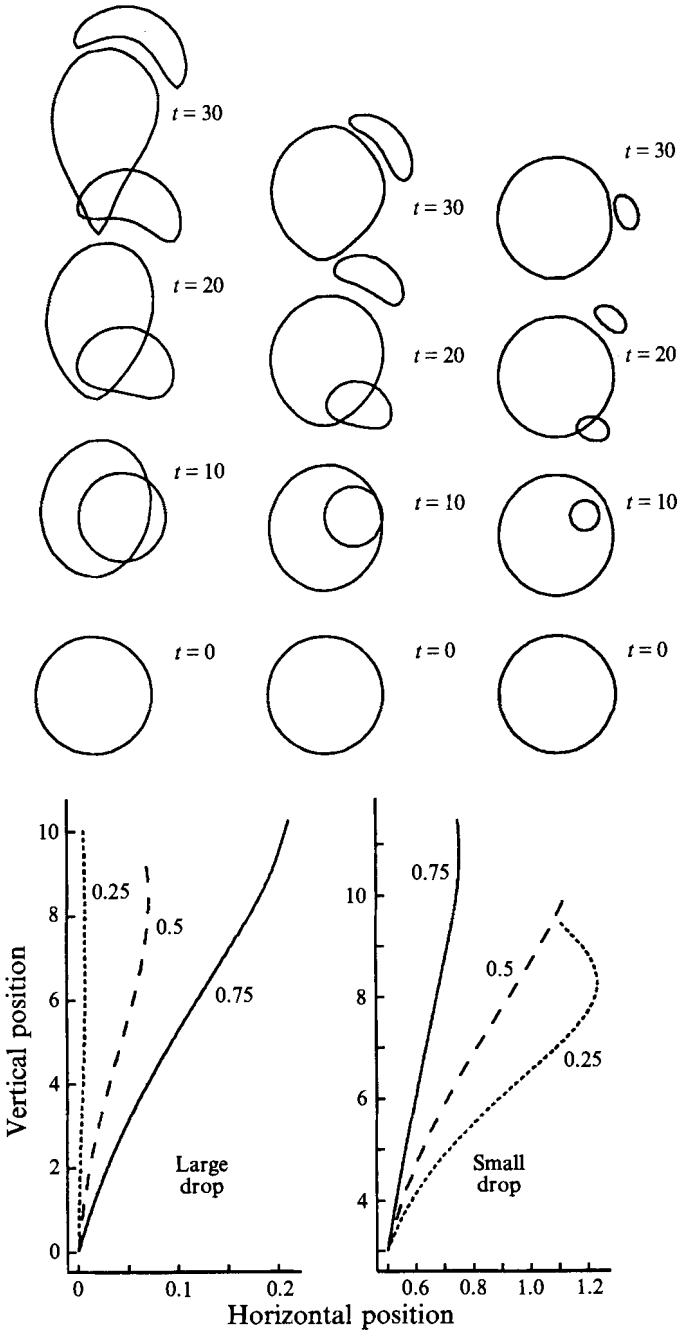

FIGURE 6. The effect of relative size on the alignment of three-dimensional offset drops for size ratios (a_2/a_1) of 0.75, 0.5 and 0.25; $\mathscr{B} = 10$, $\lambda = 1$ (Bond number based on the radius of the larger drop). Cross-sections of three-dimensional shapes are shown. Drop trajectories are shown in the lower figure.

rapidly for the $\mathscr{B} = 1$ simulation, similar to the observations for axisymmetric drops (Manga & Stone 1993), since increased deformation characteristic of larger Bond numbers requires fluid between the drops to be squeezed over a larger surface area. From the trajectories shown, we observe that the larger trailing drop for $\mathscr{B} = 100$

experiences the greatest horizontal drift, due the larger shape distortions. The effects of deformation on the trajectories of the small drops are less noticeable since the distortional contribution to the rise speed is small compared to the first reflection, equations (2.4) and (2.5).

2.5. *Effects of horizontal offset*

In figure 5 results are presented for initial horizontal offsets of $0.5a_1$, $0.9a_1$ and $1.3a_1$; $\mathscr{B} = 10$, $a_2/a_1 = 0.5$ and $\lambda = 1$. As the initial horizontal offset is increased the magnitude of deformation decreases. However, the magnitude of deformation also depends on the relative orientation of the drops and a more detailed analysis shows

$$\epsilon = O\left(|\hat{\boldsymbol{d}} \cdot \hat{\boldsymbol{g}}| \mathscr{B} \frac{a^2}{d^2}\right), \tag{2.9}$$

where $\hat{\boldsymbol{d}}$ is a unit vector joining the centres of the two drops and $\hat{\boldsymbol{g}}$ is a unit vector in the vertical direction (Manga & Stone 1993). From the drop trajectories, we observe that as the initial horizontal offset increases, the translation distance over which the large drop overtakes and passes the smaller drop decreases.

2.6. *Effects of relative drop size*

Finally, in figure 6, results are presented for size ratios $a_2/a_1 = 0.75$, 0.5 and 0.25; $\mathscr{B} = 10$ and $\lambda = 1$. The initial horizontal offsets between the centres of mass of the drops are identical in all three simulations. From the drop shapes we observe that as the relative drop size decreases, the likelihood of alignment, which is a good first indicator of coalescence, decreases: for $a_2/a_1 = 0.75$ the small drop coats the larger drop whereas for $a_2/a_1 = 0.25$ the small drop is advected around the larger drop. We also note that, as in the previous results, the magnitude of deformation of the small drop is always greater than that of the larger drop, as expected from equation (2.8). From the drop trajectories we observe that the horizontal translation of the larger drop in the simulation with $a_2/a_1 = 0.25$ is small since the contribution of the first reflection to the rise speed of the larger drop is small.

2.7. *Three drops*

In figure 7 we present calculated cross-sections of interface shapes for three different simulations of three-drop interactions, with initial conditions chosen such that all three drops lie in the vertical plane. The initial configurations are different for the three simulations, and in each case $\mathscr{B} = 10$, $\lambda = 1$, and all the drops have the same radius. In the simulation with three initially equally spaced horizontally aligned drops, the middle drop translates faster than the two outer drops. As for spherical shapes, the rise speed of the middle drop is largest owing to the sum of the first reflections characteristic of drop interactions: the first reflection for the middle drop gives rise to a $5U^{(0)}a/4d$ correction to the rise speed, whereas the rise speed correction of the outer drops is smaller, $15U^{(0)}a/16d$. The deformed drop shapes are consistent with predictions based on figure 2(*b*): the middle drop is squeezed by the flow created by the outer two drops (so that it becomes elongated in the vertical direction and extended in a direction perpendicular to the page) whereas the outer drops are extended in a direction approximately aligned with a line joining the outer drops with the middle drop.

To leading order, the magnitude of drop deformation is $O(\mathscr{B}a^2/d^2)$, but also depends on the relative orientation of the drops, as illustrated by equation (2.9). The effects of orientation are evident in the simulations in figure 7(*b*,*c*) with initially vertically offset

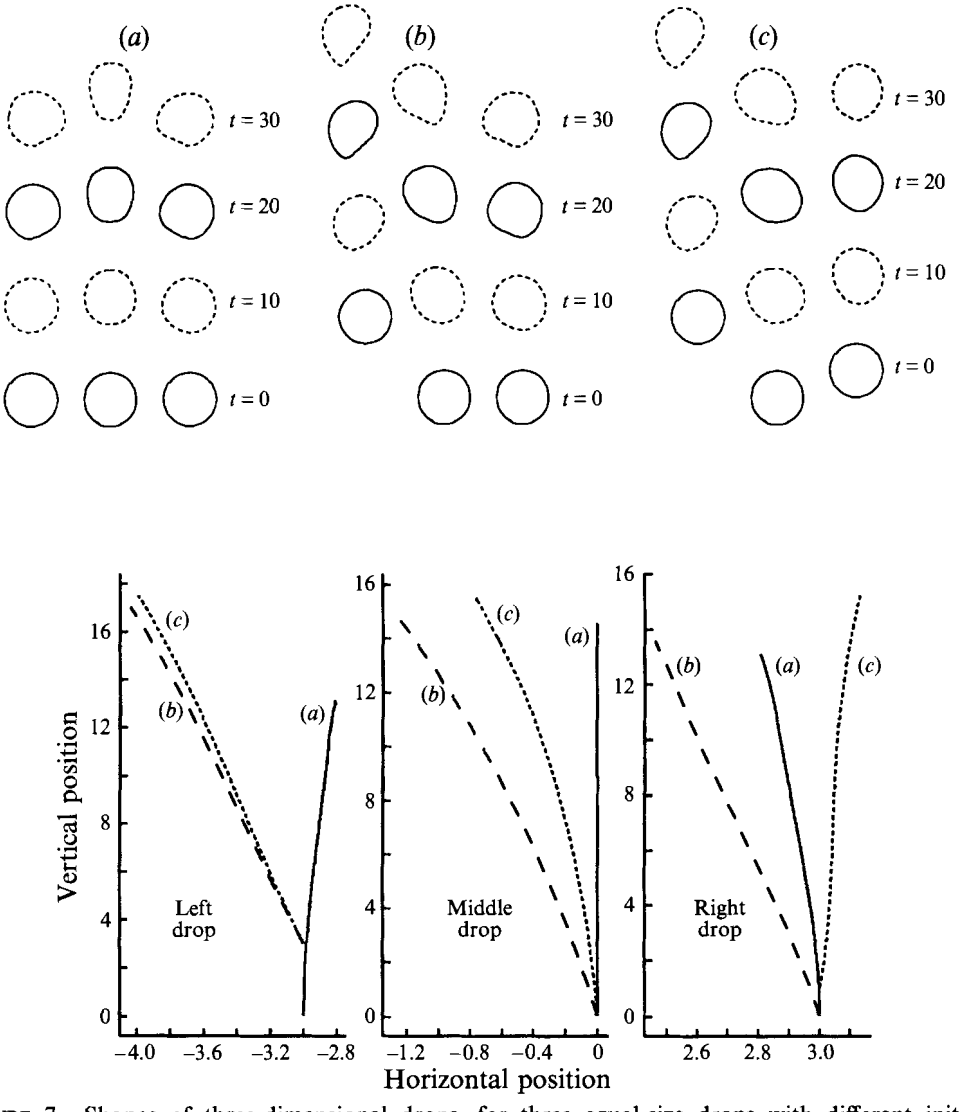

FIGURE 7. Shapes of three-dimensional drops, for three equal-size drops with different initial vertical offsets but identical horizontal offsets; $\mathscr{B} = 10$, $\lambda = 1$. Cross-sections of drop shapes are shown.

drops. In both simulations the middle drop is deformed primarily by the left drop even though the separation distance between the middle and right drop is less than the separation distance between the middle and left drop. We note that the deformed drop shapes for the middle and left drop are similar to the shapes in simulations with only two drops, such as in figure 11 (shown later). The effects of relative drop orientation on the detailed translation of the drops is highlighted by the trajectory plots: for example, contrast the opposite horizontal displacements of the right-most drop in simulations (*b*) and (*c*) for which the change of the initial vertical offset is one drop radius.

2.8. *Four drops*

In figure 8 we show three simulations of four-drop interactions, with four drops placed on the corners of a square in the vertical plane; $\mathscr{B} = 1$, 10 and 100, $\lambda = 1$.

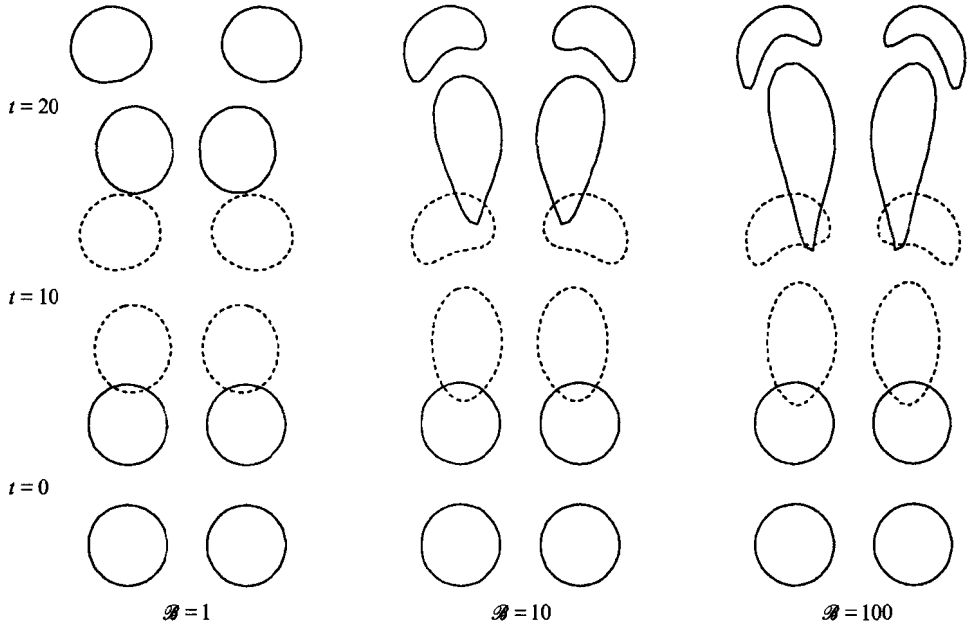

FIGURE 8. Interaction of four three-dimensional drops initially forming the sides of a square, for four equal-size drops with $\mathscr{B} = 1$, 10 and 100; $\lambda = 1$. Cross-sections of drop shapes are shown.

The evolution for four spherical particles can be deduced by considering the first reflections: the two lower spheres approach each other, the two upper spheres move away from each other, and the two lower spheres rise faster than the outer spheres so that they rise and form a horizontal line with the upper spheres; the two middle spheres continue to rise faster than the outer spheres and move apart while the two outer spheres approach each other; a configuration identical to the initial configuration will then arise; however, the lower spheres will have replaced the upper ones. The evolution of the system will continue and the motion may be described as 'leap-frogging' (e.g. Hocking 1964; Durlofsky, Brady & Bossis 1987). If the particles are deformable, the simulations shown in figure 8, the drops may coalesce without 'leap-frogging'. Again, the importance of the relative orientation of the drops on the shape and magnitude of deformation is apparent in figure 8. Qualitatively, the interaction between the right two drops is largely unaffected by the left drops (compare the simulations in figure 8 with the simulations presented later in figure 11).

Overall, the results presented in this section demonstrate that vertical offsets have a more significant influence on deformation and translation than equivalent horizontal offsets (as may be expected from the point force response, equations (2.2)–(2.3)).

3. Coalescence in suspensions

Below we provide an overview of a method for determining the evolution of particle size and concentration in dilute suspensions. The method involves first estimating the collision or coalescence rate of two particles, and then developing a population dynamics model.

3.1. *Collision-frequency function*

For a dilute suspension we make the standard approximation that only two-particle interactions need to be considered since the probability that a third particle will affect the dynamics is small. The rate at which spherical particles with radius a_i collide with particles with radius a_j is given by the collision-frequency function J_{ij} (e.g. Davis 1984)

$$J_{ij} = -n_i n_j \int_{r=a_i+a_j} p_{ij}(\boldsymbol{r})(\boldsymbol{v}_i - \boldsymbol{v}_j) \cdot \hat{\boldsymbol{r}}\, \mathrm{d}S, \tag{3.1}$$

where n_i is the number of particles of size a_i per unit volume, $p_{ij}(\boldsymbol{r})$ is the pair-distribution function which represents the probability of finding a particle of size i between $\boldsymbol{r}$ and $\boldsymbol{r} + \mathrm{d}\boldsymbol{r}$ with respect to the position of particle j, $\boldsymbol{v}_i - \boldsymbol{v}_j$ is the difference in velocities of particles with radii a_i and a_j, and $\hat{\boldsymbol{r}}$ is a unit vector in the direction of $\boldsymbol{r}$. For notational convenience we assume that a_i is the radius of the larger of the two drops.

The pair-distribution function p_{ij} satisfies a conservation equation

$$\frac{\partial p_{ij}}{\partial t} + \nabla \cdot (p_{ij}[\boldsymbol{v}_i - \boldsymbol{v}_j]) = 0. \tag{3.2}$$

In the limit that $|\boldsymbol{r}| \to \infty$, one boundary condition on the pair-distribution function is

$$p_{ij}(\boldsymbol{r}) \to 1 \text{ as } |\boldsymbol{r}| \to \infty, \tag{3.3}$$

since the suspension has particles uniformly distributed at large distances. At $r = a_i + a_j$ the drops are in contact, and are thus assumed to coalesce, so that

$$p_{ij}(\boldsymbol{r}) = 0 \text{ at } r = a_i + a_j. \tag{3.4}$$

If the particle size and number distribution remain nearly constant at a given position in the tank then we can make a quasi-steady approximation, which simplifies (3.2) to

$$\nabla \cdot (p_{ij}[\boldsymbol{v}_i - \boldsymbol{v}_j]) = 0. \tag{3.5}$$

Applying the divergence theorem to the collision-frequency equation (3.1) we find

$$J_{ij} = n_i n_j \int_{r=a_i+a_j} \nabla \cdot (p(\boldsymbol{r})_{ij}[\boldsymbol{v}_i - \boldsymbol{v}_j])\mathrm{d}V \; - \; n_i n_j \int_{r=\infty} p(\boldsymbol{r})_{ij}(\boldsymbol{v}_i - \boldsymbol{v}_j) \cdot \hat{\boldsymbol{r}}\, \mathrm{d}S. \tag{3.6}$$

The first integral vanishes identically because of the quasi-steady approximation, and the collision-frequency function simplifies to

$$J_{ij} = -n_i n_j \int_{r=\infty} (\boldsymbol{v}_i - \boldsymbol{v}_j) \cdot \hat{\boldsymbol{r}}\, \mathrm{d}S, \tag{3.7}$$

where we have applied the boundary condition on $p_{ij}(\boldsymbol{r})$ at infinity.

The collision-frequency function determined from the integral (3.7) involves an integration over the surface at infinity, S_∞, enclosing all possible drop trajectories which result in coalescence. The surface S_∞ can be described as a circle or disc of radius y_c, such that all drops with horizontal separation distances less than y_c coalesce, and all drops with horizontal separation distances greater than y_c do not coalesce (see figure 9). Neglecting the effects of deformation on the rise speed, since $\boldsymbol{v}_i - \boldsymbol{v}_j \to \boldsymbol{U}_i^{(0)} - \boldsymbol{U}_j^{(0)}$ as $r \to \infty$, the rate of coalescence is given by

$$J_{ij} = n_i n_j \pi (U_i^{(0)} - U_j^{(0)}) y_c^2. \tag{3.8}$$

It remains to determine y_c.

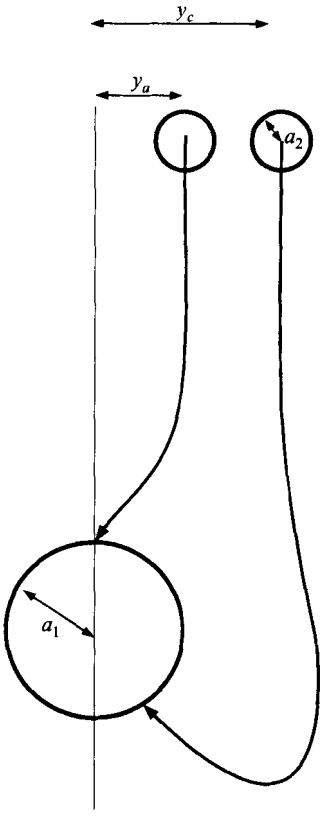

FIGURE 9. Schematic illustration of the capture radius for interacting drops. The horizontal offset y_a separates trajectories which result in alignment from those trajectories resulting in entrainment; the offset y_c separates trajectories resulting in entrainment from trajectories of bubbles which miss each other, and thus is the largest offset for which we expect coalescence.

3.2. *The Smoluchowski model*

The Smoluchowski model (Smoluchowski 1917 as cited in Davis 1984) assumes that there are no hydrodynamic interactions between particles so that the drops rise vertically, thus

$$J_{ij} = n_i n_j \pi (U_i^{(0)} - U_j^{(0)})(a_i + a_j)^2. \tag{3.9}$$

Hydrodynamically interacting spheres, as shown by previous investigators, have a reduced collision rate compared to the Smoluchowski model (even if van der Waals forces are included) since small particles tend to follow streamlines around larger particles, e.g. figure 2(*a*). However we will demonstrate that *deformable* drops not only have an enhanced rate of coalescence, but may also have a a collision rate greater than predicted by the Smoluchowski model (e.g. the experiments shown in figure 1).

4. Monodisperse suspensions

In this section we derive a result specific to monodisperse suspensions. Manga & Stone (1993) derived an expression for the translational velocity $\boldsymbol{U}$ of two widely separated drops, separated by distance d (with $d/a \gg 1$), and valid in the limit of

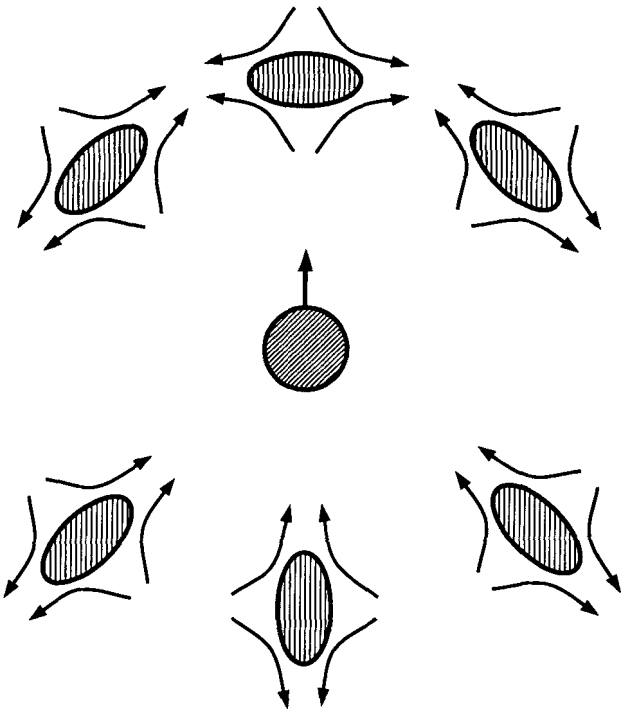

FIGURE 10. Schematic illustration of the interaction of two deformable drops in a suspension. The flow curves shown indicate the local straining motion caused by the centre drop. The effects of hydrodynamic interactions result in deformations which leads to a component of translation tending to align two drops.

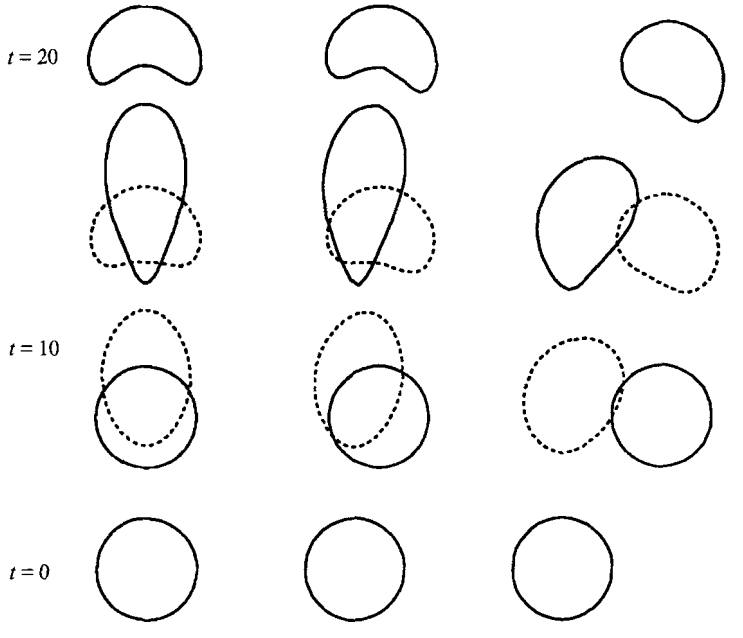

FIGURE 11. Shapes of two three-dimensional drops, for equal-size drops with different initial horizontal offsets; $\mathscr{B} = 10$, $\lambda = 1$. Cross-sections of drop shapes are shown.

small distortions, in the form

$$U = U^{(0)} + \frac{a}{d}U^{(1)} + \mathscr{B}\left(\frac{a}{d}\right)^2 U^{(2)} + O\left(U^{(0)}\frac{a^3}{d^3}\right). \tag{4.1}$$

The second term on the right-hand side is the first reflection for spherical drops. Higher-order reflections are $O(U^{(0)}a^3/d^3)$. Since the magnitude of deformation of each drop, given by equations (2.6) and (2.7), is $O(\mathscr{B}(a/d)^2)$, there will be a correction to the rise speed with magnitude $O(U^{(0)}\mathscr{B}(a/d)^2)$ represented by the third term on the right-hand side. The derivation of equation (4.1) required a quasi-steady assumption for the drop shapes, i.e. that the time for the drops to deform is shorter than the time for the two-drop geometry to change significantly. The timescale τ_d for deformation is

$$\tau_d \approx a(1+\lambda)\mu/\sigma. \tag{4.2}$$

while the timescale τ_a over which the separation distance changes is

$$\tau_a \approx \mathscr{B}\left(\frac{a}{d}\right)^2 U^{(0)}. \tag{4.3}$$

Thus, the quasi-steady assumption requires

$$\mathscr{B} < O\left(\frac{d}{a}\right)^{3/2}. \tag{4.4}$$

Since two equal-size deformable drops will always be aligned owing to the effects of deformation, as illustrated schematically in figure 10, then S_∞ is a spherical surface at infinity. Substituting the far-field analytical results derived in Manga & Stone (1993, §5) into equation (3.7) and performing the integration over the surface at $r = \infty$, we find the collision-frequency function $J(a)$ for drops with radius a in a monodisperse suspension with n drops per unit volume:

$$J(a) = 4\pi n^2 c(\lambda) a^2 \mathscr{B} U^{(0)}, \tag{4.5}$$

where the function $c(\lambda)$ is defined by equation (5.24) in Manga & Stone (1993). The linear dependence on the Bond number highlights the increased rate of coalescence produced by deformation of the microstructure. In deriving equation (4.5) we have neglected all short-range phenomena such as van der Waals forces which are required for the eventual coalescence of particles and we have assumed that the magnitude of drop distortion is small so that the perturbation expansion (4.1) is valid.

In figure 11 we demonstrate numerically using a three-dimensional boundary integral calculation that the effects of interaction lead to deformed shapes which promote alignment, and thus the coalescence of drops, even in *monodisperse* suspensions.

5. Collision frequency in polydisperse suspensions

In a polydisperse suspension, the drops have different sizes, so we need to determine the capture cross-section y_c^2 as a function of the Bond number $\mathscr{B}$, the relative drop size a_j/a_i and the viscosity ratio between the drops and surrounding fluid λ, i.e.

$$J_{ij} = n_i n_j \pi (U_i^{(0)} - U_j^{(0)}) y_c^2 \left(\mathscr{B}_i, \frac{a_j}{a_i}, \lambda\right). \tag{5.1}$$

Throughout the discussion below, we assume $a_i > a_j$ and the Bond number is based on the radius of drop i, $\mathscr{B}_i = \Delta\rho g a_i^2/\sigma$.

The complex interactions of deformable drops limit the use of analytical results and numerical studies to quantitatively determine y_c. Numerical calculations are prohibitively time consuming since many hundreds of simulations are necessary to construct a model. Furthermore, in order to estimate the capture radius y_c the initial vertical separation distance between the drops must be large, which in numerical simulations leads to long computation times. In addition, the boundary integral numerical simulations are difficult for $\lambda \neq 1$ and large interface distortions. The analytical results developed in Manga & Stone (1993) are limited to small ellipsoidal drop distortions and large separation distances. Hence, we describe an experimental approach to determine y_c for bubbles ($\lambda = 0$).

5.1. *Experimental apparatus and procedure*

In order to determine the collision frequency in a polydisperse suspension we performed a large number of laboratory experiments characterizing the interactions of air bubbles in high-viscosity corn syrup in order to develop a model for the coalescence of bubbles in dilute suspensions. The experimental results presented here consider only the limit in which large distortions occur so that the deformation, as observed in figure 1, results in the capture and coalescence of bubbles. Interfacial effects such as van der Waals forces or the presence of surfactants are important for the eventual coalescence of two bubbles; however, for large distortions, such effects will only play a minor role in the rate of coagulation of bubbles. The experiments were performed in a large Plexiglas tank with dimensions 61 cm $\times$ 61 cm $\times$ 122 cm filled with commercial grade corn syrup, $\mu = 260$ Pa s (figure 12). Bubbles were injected into the bottom of the tank through a sequence of regularly spaced holes fitted with one-way valves and the bubble volumes were measured by calibrating a series of syringes. The error in measuring bubble radius was less than 4% and is described in Appendix B. Typical bubble radii were $O(1$ cm).

In the experiments, the small bubble was injected first. In order to minimize the effects of not having an initially infinite vertical separation distance between the bubbles, the second larger bubble was injected once the small bubble had risen at least 25 cm. In order to minimize boundary effects, all interactions were required to occur at least 25 cm away from a boundary (sidewalls, the upper free-surface and the lower rigid boundary) in order to be included as acceptable data.

5.2. *Experimental results*

In figure 13, we present a series of experimental results which characterize the three different possible modes of bubble interactions for $\mathscr{B} = 120$, 73, 30 and 15. Symbols represent data and solid curves are sketched to separate the three modes of interaction. The results illustrate that for a given horizontal separation distance, y, coalescence is more likely if the bubbles have a nearly equal size than a large size difference. For a given relative size (fixed a_j/a_i, see figure 12), as the separation distance is increased: (i) the bubbles first interact such that the smaller bubble spreads over or 'coats' the larger bubble (as in figure 1*a*), (ii) as the horizontal separation distance is gradually increased, the smaller bubble may be advected around the larger bubble and then entrained inside the larger bubble (as in figure 1*b*), and finally (iii) for still greater horizontal separation distances, the smaller bubble is advected around the larger bubble and coalescence does not occur.

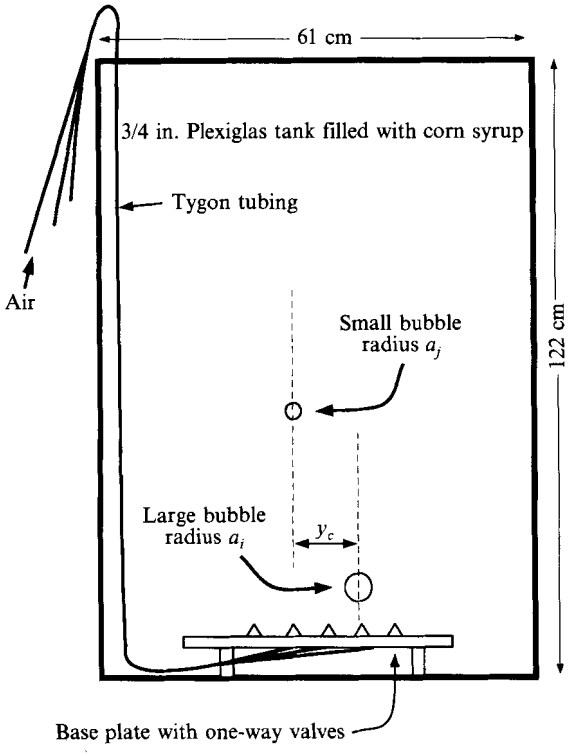

FIGURE 12. Schematic diagram of the tank used for the experiments presented in §5. The tank is made of 3/4 in. Plexiglas. Bubbles are injected from calibrated syringes into the tank through tygon tubing connected to one-way valves. The radii of the larger and smaller bubbles are a_i and a_j, respectively, and y_c is the horizontal separation distance between the bubbles which separates trajectories in which the bubbles coalesce from trajectories in which the bubbles miss each other.

In figure 14 we present experimental measurements for the dimensionless capture cross-section $y_c^2/(a_i+a_j)^2$ in equation (5.1) as a function of $\mathscr{B}_i$ and the relative bubble radius a_j/a_i, which are used to construct an approximate quantitative model for bubble coalescence. Results are presented for $\mathscr{B} = 15$, 30, 73 and 120. Solid data points indicate interactions which result in coalescence while open symbols denote interactions in which no coalescence occurs. Error bars are not shown though they are typically less than twice the size of a symbol. Data presented in figure 14 for the capture cross-section is subject to an additional constraint: specifically, in addition to the restrictions stated in §5.1, we also require that the magnitude of bubble distortion, which is predicted by far-field interactions for the measured initial separation distance, is less than 10% ($\epsilon < 0.1$ as defined by equations (2.6) and (2.7)). Hence, despite the large volume of the tank, we could only accept experimental results for a limited number of horizontal bubble separation distances, Bond numbers and relative bubble

FIGURE 13. The mode of bubble interaction as a function of bubble offset, y, and relative bubble size, a_j/a_i, for (*a*) $\mathscr{B} = 120$, (*b*) $\mathscr{B} = 73$, (*c*) $\mathscr{B} = 30$ and (*d*) $\mathscr{B} = 15$. 'Coat' refers to interactions as in figure 1(*a*) (shown with the symbol □), 'entrain' refers to interactions as in figure 1(*b*) (shown with the symbol △), and 'miss' refers to interactions in which the bubbles to not coalesce (shown with the symbol ○). The solid curves are sketched to separate the three modes of interaction. The bubbles are initially separated vertically by at least $10a_1$ in (*a,b*) and $18a_1$ in (*c,d*).

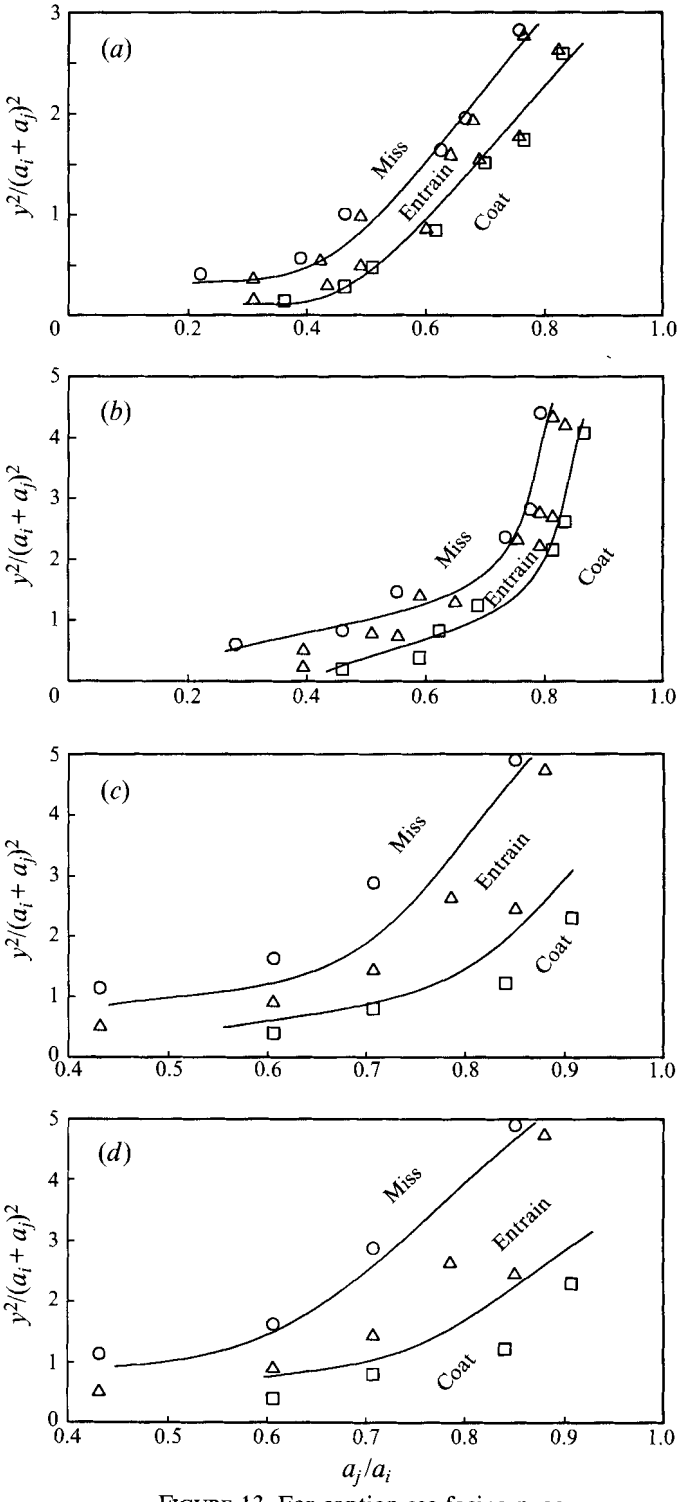

FIGURE 13. For caption see facing page.

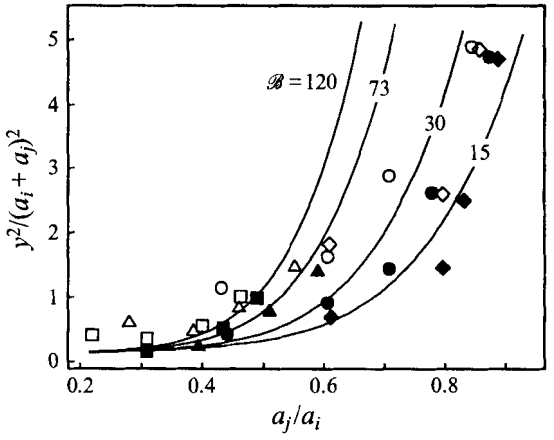

FIGURE 14. Capture cross-section as a function of $\mathscr{B}_i$ and a_j/a_i: $\mathscr{B} = 120$ (□), $\mathscr{B} = 73$ (△), $\mathscr{B} = 30$ (○) and $\mathscr{B} = 15$ (◇). Open symbols denote interactions in which the bubbles do not coalesce and solid symbols indicate interactions in which the bubbles coalesce. The solid curves represent predictions using equation (5.2).

sizes. A larger apparatus would be necessary to collect additional data for bubbles with large Bond numbers ($\mathscr{B} = 73$ and 120).

For comparison with the experimental results presented in figure 14, predictions from an empirical model of the form

$$\frac{y_c^2}{(a_i + a_j)^2} = 0.3\left(\frac{a_j}{a_i}\right)^{1/2} + \frac{1}{2}\mathscr{B}_i\left(\frac{a_j}{a_i}\right)^6 \tag{5.2}$$

are shown with solid curves for the four values of the Bond numbers. From equation (5.2), in the limit that $\mathscr{B} \to 0$ we approximately recover the result of Zhang & Davis (1991) for spherical bubbles. Equation (5.2) is *not* based on analytical results or theory, but is nevertheless a useful functional relationship between the capture cross-section, y_c^2, the Bond number, and the relative bubble size, which is approximately consistent with the experimental data presented in figure 14. Different forms of power-law fits were attempted and equation (5.2) provided the best qualitative fit to the data, in addition to being proportional to the Bond number as in equation (4.5) for monodisperse suspensions.

For reference, a capture cross-section equal to the sum of the bubble radii, $y_c^2/(a_i + a_j)^2 = 1$, corresponds to spherical bubbles moving vertically with no hydrodynamic interactions, in which case smaller bubbles are not advected around larger bubbles. From the experimental results shown in figures 13 and 14, we note that the capture cross-section may even be larger than the sum of the bubble radii (see also the experiments presented in figure 1).

The dimensionless rate of coalescence is shown in figure 15 for the model described by equation (5.1) and the experimentally determined capture cross-section modelled by equation (5.2). For comparison, analytical results for spherical bubbles ($\mathscr{B} = 0$) from Zinchenko (1982) are shown with small open circles. The rate of coalescence of deformable bubbles may be more than one order of magnitude greater than for spherical bubbles for a wide range of size ratios, e.g. $0.7 < a_j/a_i < 1$ for $\mathscr{B} = 10$. For small a_j/a_i, the effects of deformation are small (although the magnitude of deformation may be large, e.g. figure 6), and small bubbles tend to follow streamlines and are advected around larger bubbles. As $a_j/a_i \to 1$, equation (5.1) predicts no

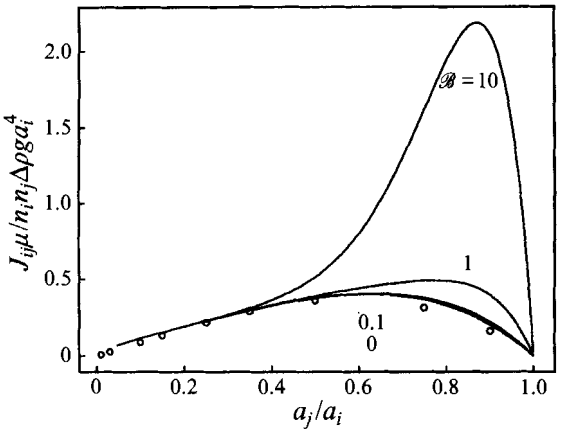

FIGURE 15. Dimensionless rate of coalescence of deformable air bubbles rising in corn syrup based on the model described by equations (5.1) and (5.2) for $\mathscr{B} = 0$, 0.1, 1 and 10. For comparison, analytical results for spherical bubbles (i.e. $\mathscr{B} = 0$) from Zinchenko (1982) are shown with open circles. Shape changes due to deformation will result in the eventual coalescence of equal-sized bubbles, thus the model described by equations (5.1) and (5.2) underestimates the rate of coalescence as $a_j/a_i \to 1$.

coalescence since the relative velocity of the bubbles $U_i - U_j \to 0$. However, as illustrated in figure 11 and discussed in §4, shape changes due to deformation will result in the eventual coalescence of equal-sized bubbles. Thus the model described by equations (5.1) and (5.2) underestimates the rate of coalescence as $a_j/a_i \to 1$.

6. Population dynamics simulations

In this section we calculate the size and concentration of buoyant deformable bubbles in dilute suspensions. We consider two problems:

(*a*) the evolution of the size distribution in an isotropic and homogeneous suspension;

(*b*) the evolution of the size distribution and concentration as a function of position in a tank of finite size.

Following the approach of Davis and coworkers (e.g. Zhang *et al.* 1993), we employ a population dynamics model based on two-bubble interactions. In the simulations we ignore any boundary or wall effects and consider only the two-particle interactions described above. Despite the limitations to the rate of coalescence equation (5.1) and the approximate nature of the experimentally based model for the rate of coalescence of deformable bubbles, equation (5.2), we apply the model developed in §5 to the two problems mentioned above. The problem of calculating dynamics in suspensions is difficult, and the results we present are based on experimental data and a theory valid for small volume fractions of bubbles, and hence capture qualitatively if not quantitatively several of the important and characteristic features of real systems.

6.1. *The population dynamics model*

We discretize the bubble size distribution into discrete intervals of bubble radii. In a homogeneous and isotropic suspension the discretized population dynamics equation which describes the rate of formation of particles of radius a_k is given by (e.g.

Friedlander 1977)

$$\frac{dn_k}{dt} = \underbrace{\frac{1}{2}\sum_{i+j=k} J_{ij}}_{\text{creation of bubbles}} - \underbrace{\sum_{i=1}^{\infty} J_{ik}}_{\text{loss of bubbles}}, \tag{6.1}$$

where n_k is the number of bubbles with radius a_k per unit volume, and J_{ij} is the collision-frequency function given by (3.1). The first term on the right-hand side of (6.1) represents the creation of bubbles with radius a_k due to coalescence of two smaller bubbles (the factor of 1/2 accounts for double counting) and the second term on the right-hand side of (6.1) represents the loss of bubbles with radius a_k due to coalescence with other bubbles.

Numerically, the bubble distribution is represented as a discrete spectrum of sizes with N bins of bubble sizes equally spaced in the logarithm of the bubble volume. The initial size distribution is assumed to be a normal distribution of the volume fraction $\phi(a)$ about an average bubble radius a_o. In all the results presented here the standard deviation characterizing the initial distribution is $0.2a_o$ (e.g. the distribution at $t = 0$ in figure 16). The total volume fraction ϕ_o of bubbles is given by

$$\phi_o = \sum_{i=1}^{\infty} \frac{4\pi}{3} a_i^3 n_i(t=0). \tag{6.2}$$

A velocity characteristic of interactions is

$$U_c = \frac{\Delta\rho g a_o^2}{\mu} \tag{6.3}$$

so that a characteristic timescale for interactions is

$$t_c = \frac{\mu}{\Delta\rho g a_o \phi_o}, \tag{6.4}$$

where $a\phi_o^{-1}$ is the typical distance between particles in a dilute suspension. Time in the simulations is normalized by t_c.

To solve equation (6.1) for homogeneous isotropic suspensions we choose a dimensionless time step of 10^{-4} and discretize the bubble size distribution so that the bubble volume doubles every 5 bins.

6.2. *Isotropic polydisperse suspensions with a homogeneous concentration distribution*

We first consider the evolution of the bubble size distribution in a suspension in which the concentration and size distribution of bubbles is initially uniform throughout the suspension and which remains uniform at all times. We refer to such a suspension as isotropic and homogeneous. This suspension may be characteristic of local dynamics for time intervals over which larger bubbles do not rise and separate from the rest of the bubbles in the suspension.

In figure 16 we show the evolution of the bubble concentration in an isotropic homogeneous suspension for different Bond numbers. The mean bubble volume as a function of time is shown in figure 17. The Bond number labelled on the curves and reported in the figure captions is based on the average initial bubble radius a_o, i.e. $\mathscr{B}_o = \Delta\rho g a_o^2/\sigma$. The detailed calculations use equation (5.1) with $\mathscr{B}_i$ based on the radius of bubble i to describe the capture cross-section so that *all* Bond numbers are included in the numerical simulations. As a result of coalescence the average bubble radius increases with time. For long times there is a noticeable influence of

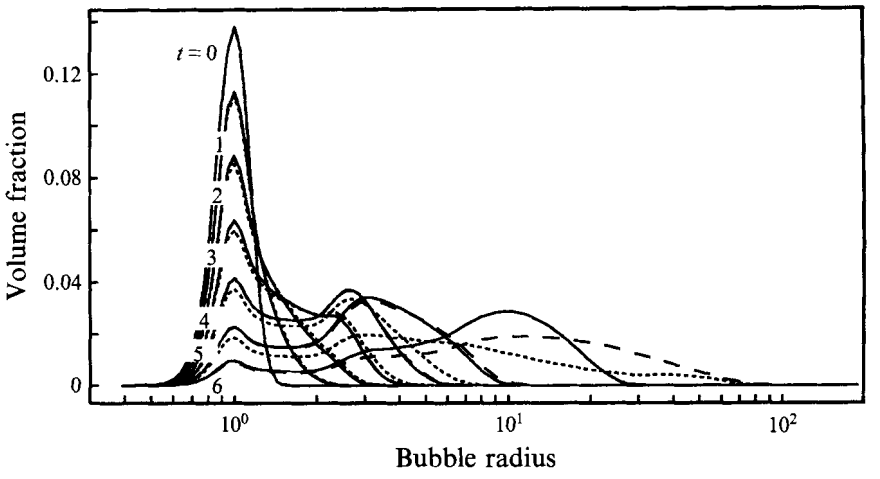

FIGURE 16. Bubble concentration in an isotropic homogeneous suspension determined by solving the population dynamics equation (6.1). The bubble distribution is shown at dimensionless times $t = 0$, 1, 2, 3, 4, 5 and 6, where time is normalized by $\mu/\Delta\rho g a_o \phi_o$. The solid curve corresponds to a simulation with $\mathscr{B}_o = 0$, the dashed curve a simulation with $\mathscr{B}_o = 0.01$, and the dotted curve a simulation with $\mathscr{B}_o = 0.1$. The Bond number is based on the average initial bubble radius a_o. The results with $\mathscr{B}_o = 0.1$ are not shown at time $t = 6$.

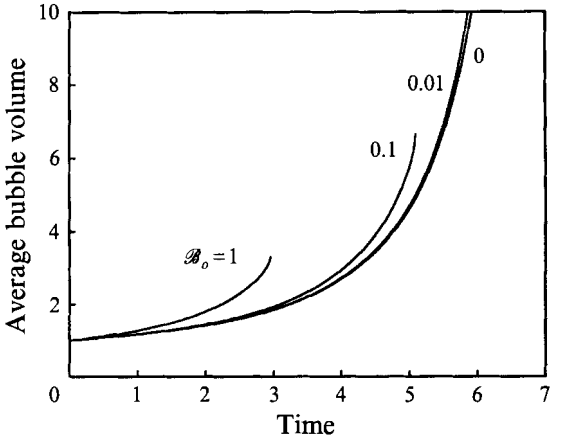

FIGURE 17. Average normalized bubble volume as a function of time in isotropic homogeneous suspension. Time is normalized by $\mu/\Delta\rho g a_o \phi_o$. Results are presented for $\mathscr{B}_o = 0$, 0.01, 0.1 and 1. The Bond number is based on the average initial bubble radius a_o.

deformation ($\mathscr{B} \neq 0$) and a wider range of bubble sizes develops in the suspension (compare the solid curve for non-deformable bubbles with the dashed and dotted curves for deformable bubbles at times $t = 5$ and 6). As the average bubble size increases, the rate of coalescence increases; since deformation enhances the rate of coalescence, the mean bubble volume in suspensions containing deformable bubbles increases more rapidly than in suspensions of spherical bubbles, as illustrated in figure 17. Finally, there is always a peak in the bubble size distribution around $a/a_o = 1$: since the rate of coalescence of bubbles becomes very small as $a_j/a_i \to 0$ (figure 15), then as the average bubble size increases due to coalescence, the smaller bubbles with $a/a_o \approx 1$ are less likely to be involved in coalescence events.

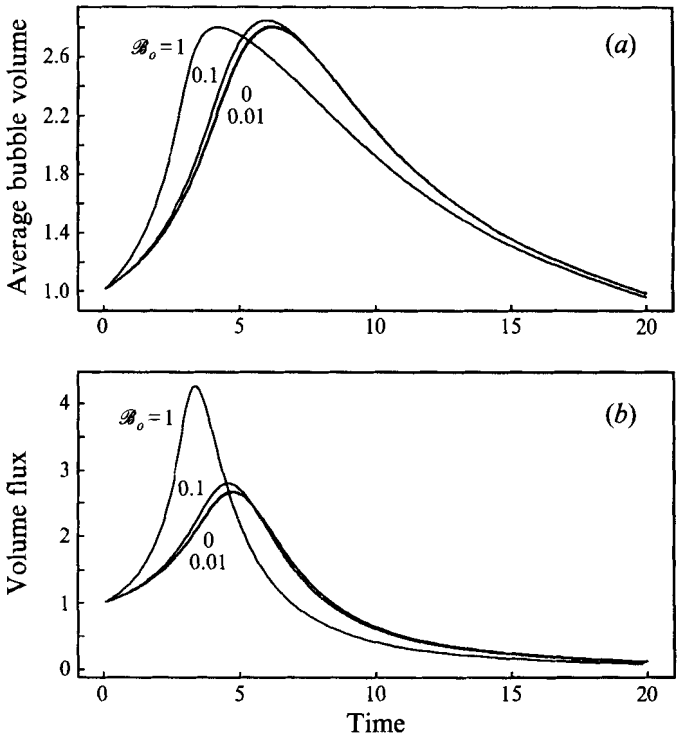

FIGURE 18. (*a*) Bubble volume at the top of a tank, measured relative to the initial average bubble volume, in an initially homogeneous suspension. Time is normalized by $\mu/\Delta\rho g a_o \phi_o$. The height of the tank is $50a_o/\phi_o$. (*b*) Volume flux of bubbles emerging from the tank, where the volume flux is normalized by the value at $t = 0$. Results are presented for $\mathscr{B}_o = 0$, 0.01, 0.1 and 1. The Bond number is based on the average initial bubble radius a_o.

The approximate model for coalescence of deformable bubbles, equation (5.2), is based on experimental results for $15 < \mathscr{B} < 120$. We might expect that the effect of deformation on the rate of coalescence saturates for large Bond numbers. Thus, in figures 16 and 17, the simulations are terminated once the Bond number of the largest bubbles exceeds 150.

The general observation in figure 16 that deformation leads to increased polydispersity is a robust qualitative conclusion which follows from the form of the rate of coalescence equation (5.2) and illustrated in figure 15. Simulations with different power laws for the capture cross-section also result in increased polydispersity.

6.3. *Coalescence and separation in a polydisperse suspension*

In suspensions the larger bubbles rise and separate from smaller bubbles, and bubbles may also leave the suspension when they reach the upper surface. Thus, we performed a number of simulations in which the bubble concentration varies with vertical position.

For the one-dimensional simulations presented below we model the dynamics by discretizing the tank height into L horizontal layers with thickness a_o/ϕ_o (Sahagian 1985). Throughout each layer bubbles of a given size are assumed to be uniformly distributed and rise with the Hadamard–Rybczyński speed $U_i^{(0)}$ based on the bubble radius a_i. The number density of bubbles of radius a_i in layer l is denoted $n_i^{(l)}$. Bubbles rise from one layer to the next, and the number density evolves according to

a discretized advective-coalescence equation

$$\text{layer } l: \quad \frac{\mathrm{d}n_i^{(l)}}{\mathrm{d}t} = \underbrace{\frac{\phi_o}{a_o} n_i^{(l-1)} U_i^{(0)}}_{\text{gain of bubbles by convection}} - \underbrace{\frac{\phi_o}{a_o} n_i^{(l)} U_i^{(0)}}_{\text{loss of bubbles by convection}} + \underbrace{\frac{1}{2} \sum_{i+j=k} J_{ij}}_{\text{creation of bubbles due to coalescence}} - \underbrace{\sum_{i=1}^{\infty} J_{ik}}_{\text{loss of bubbles due to coalescence}}. \tag{6.5}$$

In the simulations reported below we use $L = 200$; simulations with larger L produce the same results. Bubbles are initially uniformly distributed throughout the tank with volume fraction ϕ_o, and the total bubble volume fraction in layer l is calculated according to

$$\phi^{(l)}(t) = \sum_{i=1}^{\infty} \frac{4\pi}{3} a_i^3 n_i^{(l)}(t). \tag{6.6}$$

In figure 18 we demonstrate the effect of bubble deformation on the rate of separation of bubbles in a tank of height $50a_o/\phi_o$. Results are presented for $\mathscr{B}_o = 0$, 0.01, 0.1 and 1, and again the reported Bond number is based on the average initial bubble radius a_o. The rate of coalescence of bubbles is greatest for $\mathscr{B}_o = 1$. Consequently, the average bubble volume increases fastest for the system with $\mathscr{B}_o = 1$, and since larger bubbles rise more rapidly, the volume flux of bubbles out of the tank also increases most rapidly. The maximum volume flux of bubbles occurs at earlier times, and is greater, in systems with deformable bubbles than non-deformable bubbles. Thus, the rate of separation of the dispersed phase is increased by allowing the dispersed phase to deform. The importance of deformation on the rate of separation of the bubbles is highlighted in figure 19 which shows the total bubble volume fraction, equation (6.6), as a function of vertical position for deformable ($\mathscr{B}_o = 1$) and non-deformable ($\mathscr{B}_o = 0$) bubbles.

In figure 20 we concentrate on the size distribution of bubbles that exists in the top layer of the tank for $\mathscr{B}_o = 1$. The distribution is initially normally distributed about a_o. For short times, $t = 1$ and 2, coalescence shifts the size distribution to larger sizes. As the larger bubbles rise and leave the tank, the total volume fraction and the average size of the bubbles decrease. For long times (e.g. $t = 10$), the majority of bubbles left in the tank have radii less than a_o.

Finally, in figure 21 we consider the effect of tank height on the average size and rate of separation of bubbles in the tank. Results are presented for $\mathscr{B}_o = 0.1$ and tank heights $25a_o/\phi_o$, $50a_o/\phi_o$, $100a_o/\phi_o$ and $250a_o/\phi_o$. For a given volume fraction ϕ_o, the total volume of bubbles is greater in taller tanks, and the corresponding time available for interactions is longer so that larger bubbles form. Thus, the maximum volume flux of bubbles out of the tank will be larger and the maximum average volume of bubbles will also be larger in taller tanks.

6.4. *Limitations of the population dynamics simulations*

Inherent in the simulations are a large number of approximations and assumptions that may limit the applicability of the procedure described in §§6.1 and 6.3 which is used to calculate the results presented in figures 16–21: (i) The collision-frequency function and population dynamics model are applicable only in dilute suspensions for which two-particle interactions are a useful model for describing evolution of

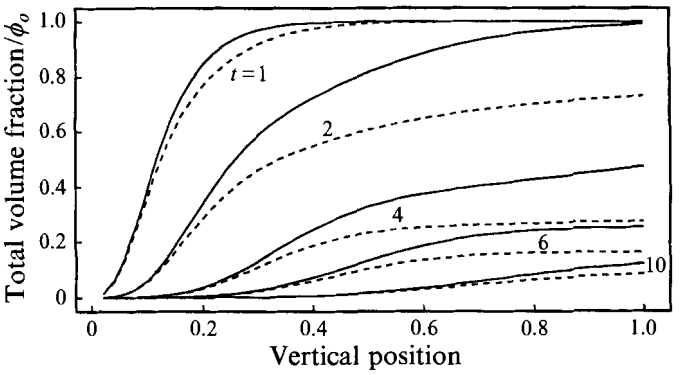

FIGURE 19. Total volume fraction of bubbles, normalized by the initial volume fraction ϕ_o, as a function of tank height (0=bottom, 1=top), at dimensionless times $t = 1$, 2, 4, 6 and 10. Results are presented for $\mathscr{B}_o = 1$ (dashed lines) and $\mathscr{B}_o = 0$ (solid lines). Time is normalized by $\mu/\Delta\rho g a_o \phi_o$. The height of the tank is normalized by $50a_o/\phi_o$. The Bond number is based on the average initial bubble radius a_o.

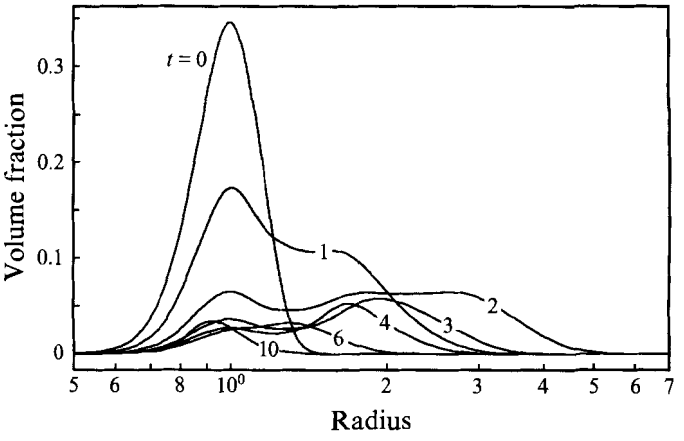

FIGURE 20. The size distribution of bubbles at the top of the tank, at dimensionless times $t = 0$, 1, 2, 3, 4, 6 and 10; $\mathscr{B}_o = 1$. Time is normalized by $\mu/\Delta\rho g a_o \phi_o$. The height of the tank is $50a_o/\phi_o$. The Bond number is based on the average initial bubble radius a_o.

the microstructure. However, the simulations reported in §2 demonstrate that the interactions between many deformable drops may be characterized qualitatively by two-drop interactions, so that the dilute limit might be less restrictive for deformable drops than for rigid particles. (ii) The collision-frequency model used in the simulations for deformable bubbles is based on a limited number of experimental data and underestimates the rate of coalescence as $a_j/a_i \to 1$. (iii) For the finite-volume tank simulations we use a one-dimensional model for the bubble distribution, which assumes that bubbles are uniformly distributed in each layer at all times and the number of bubbles advected out of a layer depends on the concentration of bubbles in the layer. The possibility that macroscopic instabilities occur is discussed in §7. (iv) Wall and boundary effects are not included. Nevertheless, because we have retained most of the important dynamics, we expect that the results presented in figures 16–21 are qualitatively representative of the evolution of bubble sizes and concentrations in dilute suspensions.

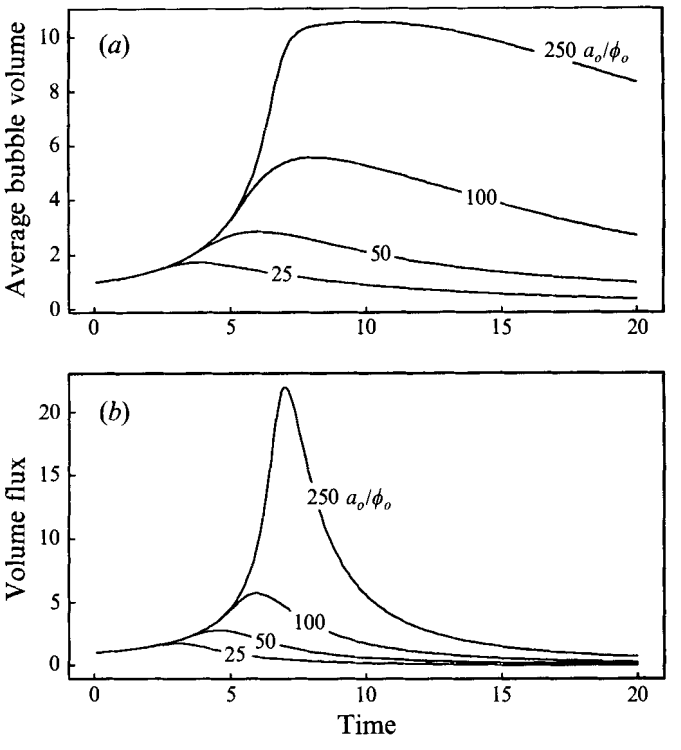

FIGURE 21. (*a*) Average normalized bubble volume of bubbles escaping from the top of a tank as a function of time in an initially homogeneous suspension. Results presented for tank heights of $25a_o/\phi_o$, $50a_o/\phi_o$, $100a_o/\phi_o$ and $250a_o/\phi_o$; $\mathscr{B}_o = 0.1$. Time is normalized by $\mu/\Delta\rho g a_o\phi_o$. (*b*) Volume flux of bubbles emerging from the tank, where again the volume flux is normalized by the value at $t = 0$.

7. Concluding remarks

On the basis of experimental results, numerical calculations, analytical estimates and population dynamics simulations, we have shown that the effects of deformation lead to an enhanced rate of coalescence of deformable drops and bubbles. The rate of coalescence in suspensions of deformable bubbles may be more than one order of magnitude greater than the rate of coalescence of non-deformable bubbles. Deformation also affects the size distribution in suspensions, resulting in a greater range of bubble sizes.

We have noted several times that the limit of dilute suspensions considered here may be less restrictive for a suspension of deformable drops than for spherical drops, and a simple geometric argument suggests why this is so. In the limit of large Bond numbers the rate of coalescence is largely governed by deformation with magnitude which decays as $(a/d)^2$ (equations (2.6) and (2.7)). However, for spherical particles, the largest interactions decay as a/d, so that the probability of a third particle affecting the dynamics will be greater. Hence, the model for coalescence presented here based on two-particle interactions should be valid for larger volume fractions of deformable drops than the comparable suspension of spherical drops.

The alignment and coalescence of bubbles may give rise to spatial inhomogeneities of bubble concentrations. For example, we might expect that bubble migration due to the deformed ellipsoidal bubble shapes will lead to spatial inhomogeneities analogous

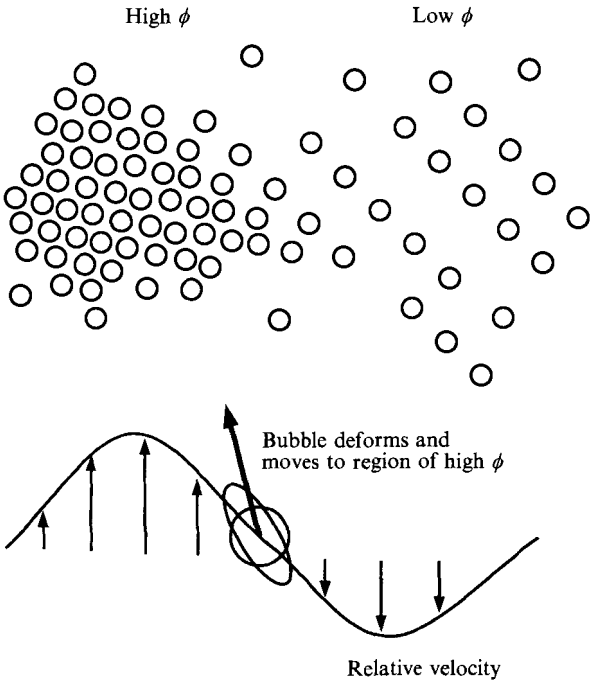

FIGURE 22. Schematic illustration of the development of spatial variations of bubble concentration (after Koch & Shaqfeh 1989). Variations of bubble concentration lead to variations of rise speed with respect to the bulk flow and thus local velocity gradients. Velocity gradients deform bubbles which then migrate from regions of lower to higher bubble concentration.

to those which develop in suspensions of ellipsoidal particles (Koch & Shaqfeh 1989). The instability arises since spatial variations of bubble concentration produce local velocity gradients which deform bubbles. Consequently, deformed bubbles migrate from a region of low to high bubble concentration, as schematically illustrated in figure 22. Based on the analysis of Koch & Shaqfeh (1989), we expect that the growth rate of the instability depends on the magnitude of bubble deformation and thus on the Bond number, and therefore we expect that larger bubbles set the lengthscale of the instability. Further work is necessary to study the development of such instabilities.

Finally, we note that the limit studied here, namely large Bond numbers and small Reynolds numbers, may be characteristic of bubbles in magmas and lavas (e.g. Sahagian 1985; Manga & Stone 1994).

This work was supported by IGPP grant 351 from Los Alamos National Lab, NSF grants CTS8957043 and EAR9218923, and the Petroleum Research Fund. C. Pozrikidis provided useful advice regarding the numerical calculations. We are especially grateful for the patience of Harvard undergraduate Joe Rice who performed most of the experiments.

Appendix A. Numerical method

Below we describe details of the numerical procedures employed in this paper to study three-dimensional free-boundary problems. A more detailed discussion is presented in Manga (1994).

In the low Reynolds number flow limit, incompressible fluid motion is governed by

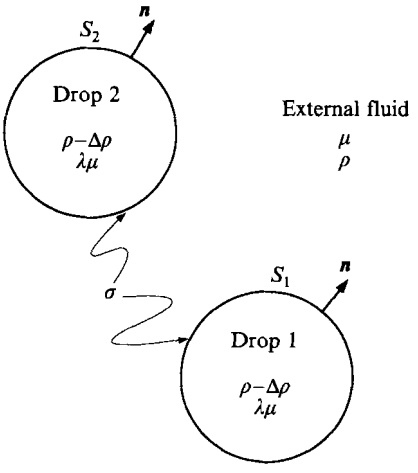

FIGURE 23. Geometry of the two-drop problem.

the Stokes and continuity equations

$$\nabla \cdot \boldsymbol{T} = -\nabla p + \mu \nabla^2 \boldsymbol{u} + \rho \boldsymbol{g} = \boldsymbol{0}, \tag{A 1}$$

$$\nabla \cdot \boldsymbol{u} = 0, \tag{A 2}$$

where $\boldsymbol{u}$ is the velocity, p is the pressure, μ and ρ are the fluid viscosity and density, respectively, and $\boldsymbol{g}$ is the gravitational acceleration. Here the stress tensor $\boldsymbol{T}$ is defined to include the hydrostatic body force in order to define a divergence-free field,

$$\boldsymbol{T} = -(p - \rho \boldsymbol{g} \cdot \boldsymbol{r})\boldsymbol{I} + \mu \left[\nabla \boldsymbol{u} + (\nabla \boldsymbol{u})^T\right], \tag{A 3}$$

where $\boldsymbol{r}$ is a position vector.

Consider a problem involving two drops, as illustrated in figure 23. We use the subscript *ext* to denote the external fluid, and the subscripts 1 and 2 to denote drops 1 and 2, respectively. We require that the velocity decays to zero far from the drops,

$$\boldsymbol{u}_{ext} \to \boldsymbol{0} \text{ as } |\boldsymbol{r}| \to \infty, \tag{A 4}$$

and that the velocity is continuous across all interfaces,

$$\boldsymbol{u}_1 = \boldsymbol{u}_{ext} \text{ on } S_1 \quad \text{and} \quad \boldsymbol{u}_2 = \boldsymbol{u}_{ext} \text{ on } S_2, \tag{A 5}$$

where S_i is the surface bounding drop i. The stress jump $[\![\boldsymbol{n} \cdot \boldsymbol{T}]\!]_i$ across interface i is balanced by the density contrast and interfacial tension stresses, which depend on the local curvature $\nabla_s \cdot \boldsymbol{n}$ of the interface:

$$[\![\boldsymbol{n} \cdot \boldsymbol{T}]\!]_1 = \boldsymbol{n} \cdot \boldsymbol{T}_{ext} - \boldsymbol{n} \cdot \boldsymbol{T}_1 = \sigma\,(\nabla_s \cdot \boldsymbol{n})\boldsymbol{n} + \boldsymbol{n}\Delta\rho \boldsymbol{g} \cdot \boldsymbol{r} \quad \text{on } S_1, \tag{A 6}$$

$$[\![\boldsymbol{n} \cdot \boldsymbol{T}]\!]_2 = \boldsymbol{n} \cdot \boldsymbol{T}_{ext} - \boldsymbol{n} \cdot \boldsymbol{T}_2 = \sigma\,(\nabla_s \cdot \boldsymbol{n})\boldsymbol{n} + \boldsymbol{n}\Delta\rho \boldsymbol{g} \cdot \boldsymbol{r} \quad \text{on } S_2, \tag{A 7}$$

where σ denotes the constant interfacial tension, $\boldsymbol{n}$ is the unit normal directed into the external fluid, and $\nabla_s = (\boldsymbol{I} - \boldsymbol{nn}) \cdot \nabla$ is the gradient operator tangent to the interface. Additionally there is a kinematic constraint, which requires that a fluid element on a fluid–fluid interface remain on that interface for all time. Formally, the kinematic constraint may be expressed with the Lagrangian description

$$\frac{\mathrm{d}\boldsymbol{r}}{\mathrm{d}t} = \boldsymbol{u}(\boldsymbol{r}) \qquad \text{for } \boldsymbol{r} \in S_1, S_2. \tag{A 8}$$

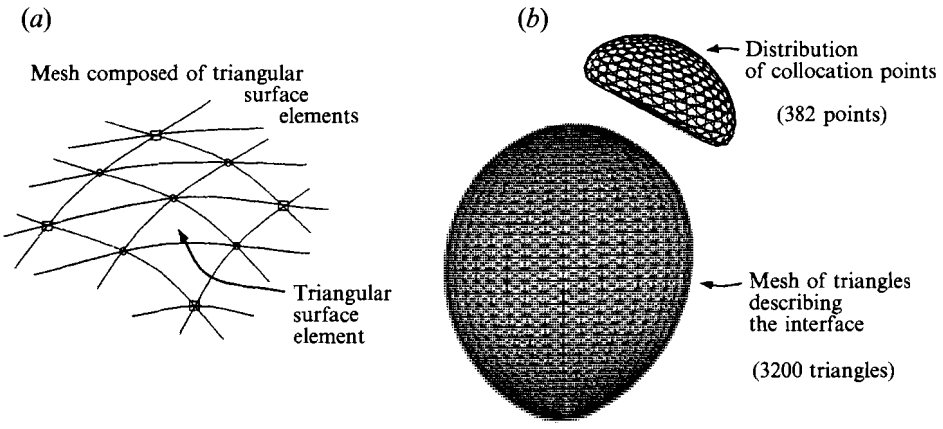

FIGURE 24. (*a*) The interface is described by a mesh of triangles, with vertices shown by open circles. Collocation points at which interfacial velocities are evaluated describe a coarser mesh, shown with open squares. (*b*) Example of a numerical mesh consisting of 382 collocation points (vertices of the triangles in top drop) and 3200 triangular surface elements (bottom drop). The mesh shown is from a typical two-drop calculation after 250 time steps, in which the large drop has translated more than 7 drop radii and the small drop has translated more than 10 drop radii. Notice that the collocation points (top drop) and triangular surface elements (bottom drop) remain well-distributed (we redistribute collocation points and triangles every 3 time steps).

Stokes equations may be recast as integral equations for the interfacial velocities. In particular, integral equations of the second kind may be derived for problems involving multiple fluid–fluid interfaces (Tanzosh, Manga & Stone 1992). The integral equations for a pair of fluid–fluid interfaces are given by

$$\frac{1}{\mu}\int_{S_1}[\![\boldsymbol{n}\cdot\boldsymbol{T}]\!]_1\cdot\boldsymbol{J}\,\mathrm{d}S-(1-\lambda)\int_{S_1}\boldsymbol{n}\cdot\boldsymbol{K}\cdot\boldsymbol{u}\,\mathrm{d}S-\frac{1}{\mu}\int_{S_2}[\![\boldsymbol{n}\cdot\boldsymbol{T}]\!]_2\cdot\boldsymbol{J}\,\mathrm{d}S,$$

$$-(1-\lambda)\int_{S_2}\boldsymbol{n}\cdot\boldsymbol{K}\cdot\boldsymbol{u}\,\mathrm{d}S=\begin{cases}\boldsymbol{u}(\boldsymbol{r}), & \boldsymbol{r}\in V_{ext},\\ \lambda\boldsymbol{u}(\boldsymbol{r}), & \boldsymbol{r}\in V_1,\\ \lambda\boldsymbol{u}(\boldsymbol{r}), & \boldsymbol{r}\in V_2,\\ \frac{1}{2}(1+\lambda)\boldsymbol{u}(\boldsymbol{r}), & \boldsymbol{r}\in S_1,\\ \frac{1}{2}(1+\lambda)\boldsymbol{u}(\boldsymbol{r}), & \boldsymbol{r}\in S_2,\end{cases}\tag{A 9}$$

where $\boldsymbol{J}$ and $\boldsymbol{K}$ are known kernels for velocity and stress, respectively (Pozrikidis 1992).

In this paper we consider only $\lambda = 1$, and solve (A9) numerically using a collocation approach. Fluid–fluid interfaces are represented numerically by a grid of $2N \times M$ triangular surface elements and the interfacial velocities are calculated on a grid of $n \times m$ collocation points, where $n < N$ and $m < M$ (see figure 24). In effect, two separate numerical meshes are employed: a high-resolution mesh to describe the surface and perform integrations (composed of 3200 triangular elements), and a second mesh at which velocities are calculated (consisting of 382 collocation points). The use of two meshes was found to be the most computationally efficient method to achieve a given accuracy. The surface normal, local curvature, and the stress jump are assumed to vary linearly over each surface element. Interfacial velocities are interpolated linearly between collocation points. Numerical integration is performed using 7-point Gaussian integration. Since the Green's functions or kernels for Stokes

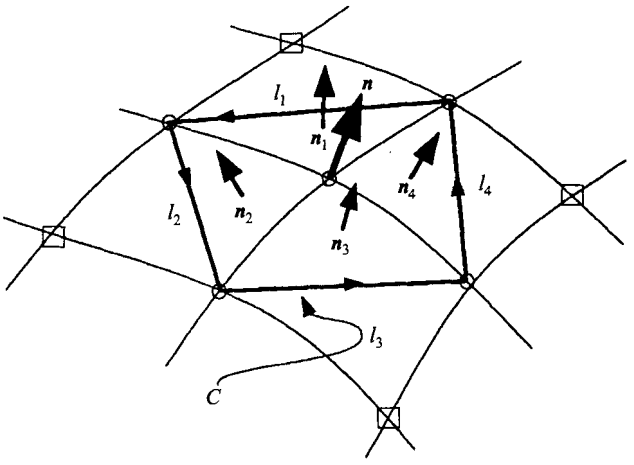

FIGURE 25. Calculating interfacial tension stresses by contour integration. The unit normal vectors to the four triangular surfaces $\boldsymbol{n}_i$ surrounding the point of interest are calculated and then averaged to calculate $\boldsymbol{n}$. The interfacial tension stresses are calculated by integrating the unit tangent vector $\boldsymbol{t} = \boldsymbol{l} \wedge \boldsymbol{n}$ times the interfacial tension around the closed contour C composed of the segments $l_1 + l_2 + l_3 + l_4$ (Pozrikidis 1994).

flows are singular, triangular surface elements containing a singularity are integrated analytically using expressions given by Rallison (1981) for linear elements.

An Euler time step is used to update the interface shape – once the interfacial velocities are calculated the position of the interface is advected with the local velocity field. We use 1000 time steps in the simulations reported here.

We estimate the normal at all vertices of the triangular surface elements by averaging the normals to all the triangular surface elements adjacent to the vertex. The interfacial tension stresses can then be evaluated by performing a contour integral around the point of interest (following Pozrikidis 1994)

$$\int_S \boldsymbol{n}(\nabla_s \cdot \boldsymbol{n}) \mathrm{d}S = -\oint_C \boldsymbol{t} \mathrm{d}l \tag{A 10}$$

where $\boldsymbol{t} = \boldsymbol{l} \wedge \boldsymbol{n}$ is a unit vector tangent to the surface S which is perpendicular to the counterclockwise contour C (see figure 25 for a definition of $\boldsymbol{l}$, $\boldsymbol{n}$ and C). The contour integration is performed using a trapezoidal rule. The curvature could be calculated to machine precision for spheres and to within 2% for ellipsoids with aspect ratios 3:1. Typically this approach to calculating the curvature underestimates it in regions of high curvature owing largely to approximating the surface with linear elements.

Since the initial interface shapes are always spherical, we distribute collocation points along lines of latitude and longitude. Thus, the concentration of collocation points is greatest near the poles. During the evolution of the interface shape the collocation points are redistributed at every third time step since they tend to accumulate near stagnation points.

For a spherical drop, interfacial velocities differ by less than 0.15% from the Hadamard–Rybczyński result. In Manga (1994) the numerical methods used here produced results which were visually indistinguishable when compared with previous axisymmetric numerical calculations for two buoyancy-driven drops and the relaxation of an initially extended drop. The steady deformation of drops in a shear flow was

calculated and found to be in agreement with results calculated by Kennedy *et al.* (1993).

Appendix B. Experimental uncertainties

The syringes used to inject the bubbles are calibrated so that the equivalent (undeformed) radius of the bubbles can be determined from the volumes of air injected from the syringe into the tank. Since air is compressible and the tubing is long, the volume of air initially contained in the syringe is always greater than the volume of the bubble. A single air bubble is injected into the tank and the rise speed is measured when the bubble is far from any boundary. Typical uncertainties of the bubble rise speed, based on 10 experiments for a given syringe volume, are less than 1%.

The bubble radius may be determined using the Hadamard–Rybczyński formula. The uncertainties of the fluid viscosity and density contrast are less than 2% and 1%, respectively. Thus the uncertainty of the bubble radius will be less than about 3–4%. However, once a rise speed can be associated with a given syringe volume, the uncertainty of the relative bubble radii, a_j/a_i as discussed in §5, can be determined independent of the fluid viscosity and density. Typical uncertainties of a_j/a_i are about 1%.

REFERENCES

DAVIS, R. H. 1984 The rate of coagulation of a dilute polydisperse system of sedimenting spheres. *J. Fluid Mech.* **145**, 179–199.

DEBRUIJN, R. A. 1989 Deformation and breakup of drops in simple shear flows. PhD thesis, Technical University at Eindhoven.

DURLOFSKY, L., BRADY, J. F. & BOSSIS, G. 1987 Dynamic simulation of hydrodynamically interacting particles. *J. Fluid Mech.* **180**, 21–49.

FRIEDLANDER, S. K. 1977 *Smoke, Dust and Haze: Fundamentals of Aerosol Behavior.* John Wiley & Sons.

HOCKING, L. M. 1964 The behaviour of clusters of spheres falling in a viscous fluid. Part 2. Slow motion theory. *J. Fluid Mech.* **20**, 129–139.

KENNEDY, M. R., POZRIKIDIS, C. & SKALAK, R. 1994 Motion and deformation of liquid drops, and the rheology of dilute emulsions in simple shear flow. *Computers Fluids* **23**, 251–278.

KOCH, D. L. & SHAQFEH, E. S. G. 1989 The instability of a dispersion of sedimenting spheroids. *J. Fluid Mech.* **209**, 521–542.

MANGA, M. 1994 The motion of deformable drops and bubbles at low Reynolds numbers: Applications to selected problems in geology and geophysics. PhD thesis, Harvard University.

MANGA, M. & STONE, H. A. 1993 Buoyancy-driven interactions between deformable drops at low Reynolds numbers. *J. Fluid Mech.* **256**, 647–683.

MANGA, M. & STONE, H. A. 1994 Interactions between bubbles in magmas and lavas: Effects of deformation. *J. Volcanol. Geothermal Res.* **63**, 269–281.

NEVERS, N. DE & WU, J.-L. 1971 Bubble coalescence in viscous fluids. *AIChE J.* **17**, 182–186.

POZRIKIDIS, C. 1992 *Boundary Integral and Singularity Methods for Linearized Viscous Flow.* Cambridge University Press.

POZRIKIDIS, C. 1994 Effects of surface viscosity on the finite deformation of a liquid drop and the rheology of dilute emulsions in simple shearing flow. *J. Non-Newtonian Fluid Mech.* **51**, 161–178.

RALLISON, J. M. 1981 A numerical study of the deformation and burst of a viscous drop in general shear flows. *J. Fluid Mech.* **109**, 465–482.

SAHAGIAN, D. L. 1985 Bubble migration and coalescence during the solidification of basaltic lava flows. *J. Geol.* **93**, 205–211.

SATRAPE, J. V. 1992 Interactions and collisions of bubbles in thermocapillary motion. *Phys. Fluids* A **4**, 1883–1900.

TANZOSH, J., MANGA, M. & STONE, H. A. 1992 Boundary element methods for viscous free-surface flow problems: Deformation of single and multiple fluid-fluid interfaces. In *Boundary Element Technolgies* (ed. C. A. Brebbia & M. S. Ingber), pp. 19–39. Computational Mechanics Publications and Elsevier Applied Science, Southampton.

UNVERDI, S. O. & TRYGGVASON, G. 1992 A front-tracking method for viscous, incompressible, multi-fluid flows. *J. Comput. Phys.* **100**, 25–37.

ZHANG, X. & DAVIS, R. H. 1991 The rate of collisions due to Brownian or gravitational motion of small drops. *J. Fluid Mech.* **230**, 479–504.

ZHANG, X., WANG, H. & DAVIS, R. H. 1993 Collective effects of temperature gradients and gravity on droplet coalescence. *Phys. Fluids* A **5**, 1602–1613.

ZINCHENKO, A. Z. 1982 Calculations of the effectiveness of gravitational coagulation of drops with allowance for internal circulation. *Prikl. Mat. Mech.* **46**, 58–65.